Characterization of Gamma Prime Precipitates in a Powder Metallurgy Nickel-Based Superalloy

By

Gabriel R. Tellier

A thesis submitted to

The Faculty of Graduate Studies

In partial fulfillment of the requirements for the degree of

MASTER OF SCIENCE

Department of Mechanical Engineering

The University of Manitoba

Winnipeg, Manitoba

September 2017

Table of Contents

List of Figures

List of Tables

List of Equations

List of Abbreviations

PM: Powder Metallurgy

HIP: Hot Isostatic Press

CIP: Cold Isostatic Pressing

FCC: Face Centered Cubic

TCP: Topologically Close Packed

SEM: Scanning Electron Microscope

TEM: Transmission Electron Microscope

SE: Secondary Electrons

BSE: Backscattered Electrons

EDS: Energy Dispersive Spectroscopy

WDS: Wavelength Dispersive Spectroscopy

AFM: Atomic Force Microscope

TAS: Ternary-Aluminium-Silicon; the main alloy used in this thesis (see Section 4.1)

DSC: Differential Scanning Calorimeter

TRS: Transverse Rupture Strength

EDM: Electrical Discharge Machining

HT: Heat Treatment

Acknowledgments

The author would like to thank Dr. W.F. Caley and Dr. N.L. Richards for their unwavering support, without which this project would not have been possible. Sincere thanks for technical assistance also go out to Dwayne Chrusch (University of Manitoba), Clark Murray (Dalhousie University) and Mike Boskwick (University of Manitoba) for their generous technical assistance.

Abstract

Nickel-based superalloys see wide use in applications where materials must maintain high strengths at high temperatures. A notable example is the use of these superalloys in the blades of gas turbines, both in the power generation and transportation industries.

One of the main sources of the superior high-temperature strength of nickel-based superalloys is the presence of Gamma Prime precipitates. These precipitates resist dislocation motion, and thus enable the superalloy to resist creep at high temperatures.

This project concentrates on characterizing the behaviour of a powder-metallurgy nickel-based superalloy consisting of Ni-12Cr-9Fe (w/o) with the addition of 6w/o Al and 0.5w/o Si. More specifically, the goal is to be able to better predict and thus control the precipitate size in order to achieve finer control of the material properties.

The JMatPro software allowed pre-experimentation modeling of the solutionization temperature of Gamma Prime in this alloy (1040˚C), which was further refined using a Differential Scanning Calorimeter to obtain an experimental value of 1092˚C. Through analysis of sample hardnesses after various heat treatments, precise temperature control was found to be more important to control material properties than exact ageing times. Using an Atomic Force Microscope, precipitates from quenched samples could be imaged (down to <40nm scales). These images were then characterized using ImageJ image processing software, and analyzed. Lastly, a thermo-mechanical deformation procedure was found to increase the sample density by a small amount (3.6% - 5.3%), and to be limited to a 30% deformation before sample rupture.

1. Introduction

Used heavily for both transportation and power-generation purposes, gas turbines are an integral part of the modern industrial landscape. As fuel efficiency becomes ever more important, higher operating temperatures are desired. This then creates a need for materials suitable for sustained use under high loading in an oxidizing atmosphere at high temperature.

“Superalloys”, or “high-performance alloys” are well suited for use in those adverse condition. Usually nickel- or cobalt-based, these superalloys resist creep deformation, maintain their superior mechanical strength at high temperatures, and are resistant to corrosion and oxidation. An important factor in the strength and creep resistance of modern nickel-based superalloys is the presence of Gamma Prime precipitates to impede dislocation motion.

This thesis attempts to better understand the behaviour of the Gamma Prime precipitates in a nickel-based powder metallurgy alloy similar to Inconel 600, to enable better control of the precipitates and thus the material properties of the alloy.

2. Background and Literature Review

This section deals with theory and background knowledge of the behaviour of powder metallurgy nickel-based alloys, as well as the processing methods and analysis techniques used. Details on the equipment used as well as the operational parameters and other practical aspects can be found in Section 4: Materials and Methods.

2.1. Powder Metallurgy

Although a less widespread technique than casting or forging, Powder Metallurgy (PM) nonetheless has been used throughout history. One of the earliest documented cases of the use of powder metallurgy was the use of iron powder by Egyptians back to 3000 BCE. On another continent, the 6.5 ton Delhi Column in India was also manufactured from iron powder circa 300 CE. More recently, the nineteenth century saw powder metallurgy being used for the manufacture of platinum laboratory apparatus, where high temperatures were avoided through the use of chemically precipitated powders (platinum melts at approximately 1768 ˚C) [1] as well as new consolidation methods. This development continued on with William Coolidge, who was instrumental in the development of the tungsten lamp filament and is considered by some to have begun the modern era of powder metallurgy. [2] (p5)

2.1.1. Advantages and Weaknesses of Powder Metallurgy

The creation of parts through PM processes has several significant advantages over traditional methods such as casting or forging. The rapid solidification and fast cooling rates achievable through powder manufacture can reduce elemental segregation, resulting in smaller-scale morphology and reduced interdendritic spacing compared with casting processes. As a corollary, the powder is uniform on the "micro" scale, resulting in outstanding property uniformity. Powder metallurgy allows the creation of unique structures tailored to their environment, such as oxide-dispersion-strengthened alloys, that cannot be created through any other method. Lastly, with proper PM process control, it is possible to create net or near-net shape products, economizing on both material and required post-processing. [3]

On the other hand, every method has its weakness. High-stress PM components such as fatigue-limited parts can be very sensitive to low defect levels from contaminants, with ensuing performance degradation. Some PM components therefore require some form of thermomechanical processing to ensure neutralization of these contaminant defects, with an attendant cost increase. On the input side of the stream, PM processes require very fine powders (leading to reduced powder yield) to control the maximum defect size, as well as careful process control. [3] As an example, the supplier Alpha Aesar offers powders with sizes ranging from 0.2nm to 1.27mm [4].

The limiting factor in application of PM components for turbine use is the defect-degraded fatigue life. [3] (p491)

2.1.2. Powder Fabrication Methods

As powder metallurgy requires the use of various types and sizes of powders, the powders must of course be produced. The most common method used for production of PM feedstock is known as “atomization fabrication”, for which there are several techniques. These techniques allow better control of the powder chemistry and shape characteristics, in both elemental and pre-alloyed form. Regardless of the actual technique used, the atomization processes involve the formation of powder from molten metal using a spray of droplets. The main advantages of this family of techniques is easy process control, as well as their inherent adaptability, allowing application to several alloys, as well as flexibility in feedstock, melt purification and alloy chemistry parameters. [2]

The most widely used atomization technique is inert gas atomization. As seen in Figure 1 below, a pressurized inert gas is directed through nozzles at a stream of molten metal, breaking up the stream into droplets as per Figure 2 below.

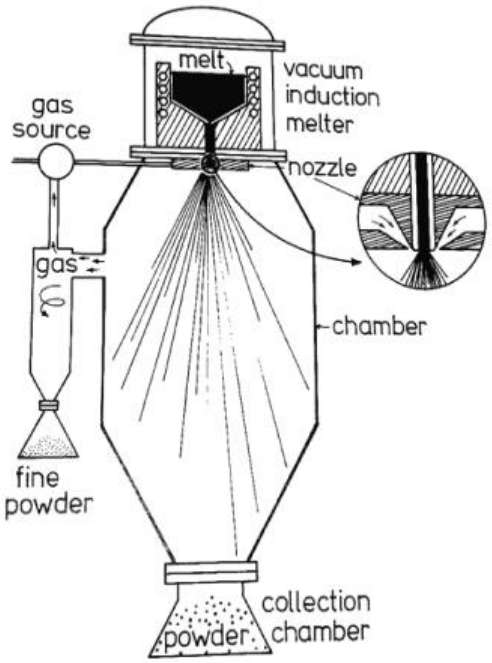

Figure 1: Typical schematic of a vertical gas atomizer [2]

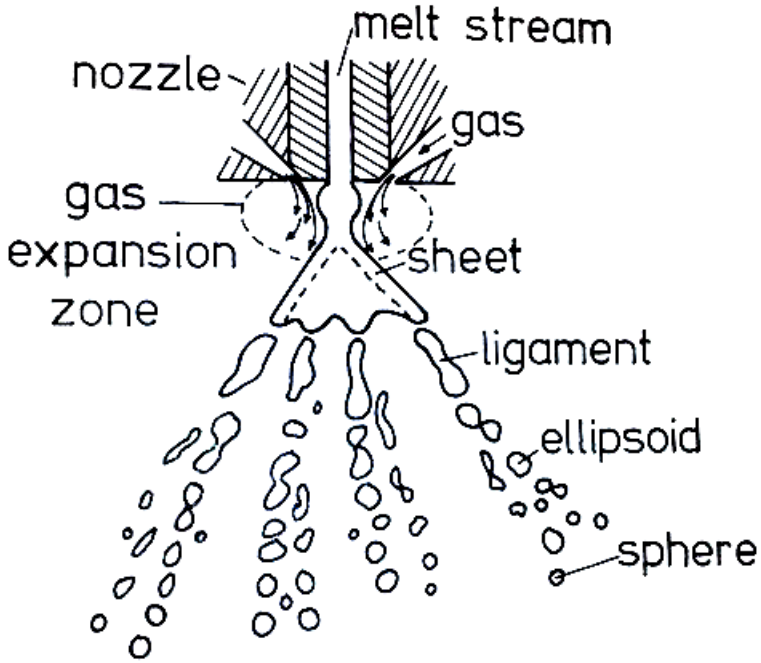

Figure 2: Formation of metal powder by gas atomization [2]

Other common methods of atomization include water-spray atomization, centrifugal atomization, and melt explosion atomization. Non-atomization techniques in use include ball milling and other mechanical impaction methods, electrolytic fabrication of high-purity powders, and chemical or thermal decomposition of oxides or other metallic compounds. [2]

2.1.3. Consolidation

Prior to the critical sintering operation, the powder or powders must be properly mixed and homogenized. In processes other than the Hot Isostatic Press (HIP) process, the powder must be compressed into "green" (unsintered) bodies to allow handling and introduction to the sintering furnace.

2.1.3.1. Pre-compaction

Lubrication is often added prior to mixing, both to enhance mixing and to improve powder flow and packing properties. Lubrication between the powder and the die wall minimizes die wear and eases ejection from the die. [2] One method of lubrication is the addition of small amounts of organic wax prior to mixing. To avoid contamination of the final product, the green bodies must be delubricated prior to sintering. [5]

Prior to the compaction of a green body, the powders must be mixed to ensure homogeneity and avoid powder segregation. As can be seen in Figure 3 below, the three modes of powder mixing are diffusion, convection, and shear mixing. All three contribute to the homogenization sequence, with varying importance depending on the mixing apparatus. [2]

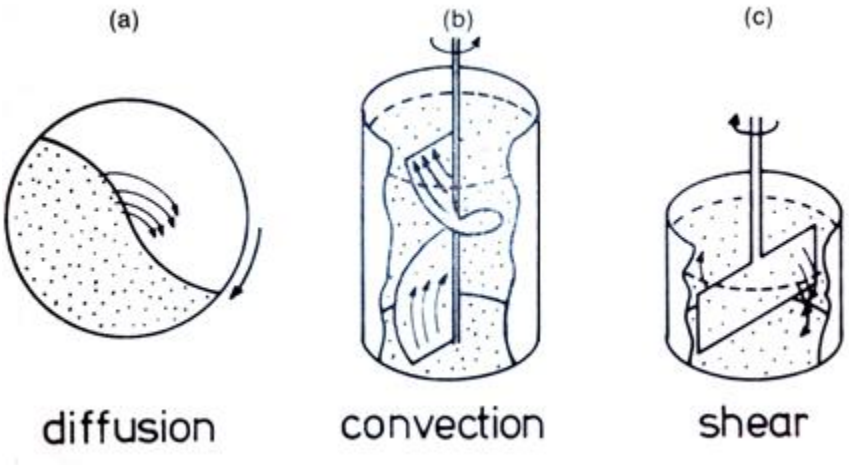

Figure 3: Three modes of powder mixing [2]

2.1.3.2. Compaction

The compaction and consolidation can be achieved through various processes such as die compaction, as well as HIP or Cold Isostatic Pressing (CIP). Uniaxial die compaction is the most common technique used, as it offers relatively low capital and maintenance costs, good dimensional tolerance, and high production rates when compared with other forms of compaction such as CIP. [2]

For uniaxial die compaction, the powder(s) are poured into a die, and compressed linearly. This process is shown in Figure 4 below. The use of multiple punches can reduce density disparities and increase the homogeneity of the green body, as seen in Figure 5 below.

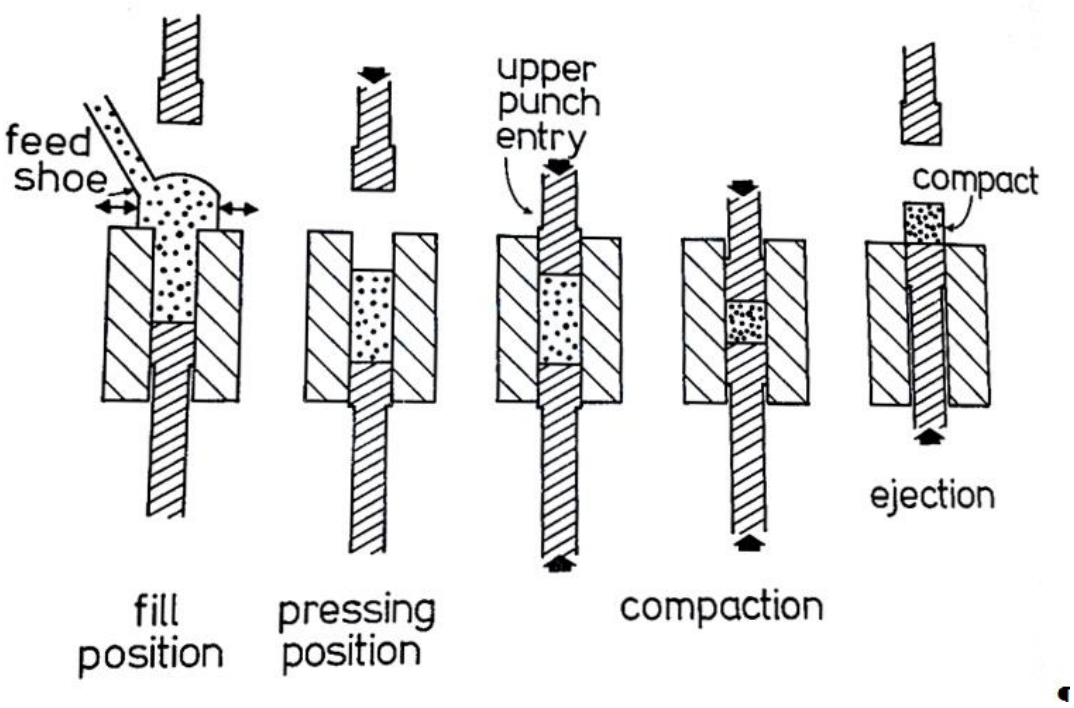

Figure 4: Typical powder uniaxial powder compaction cycle [2]

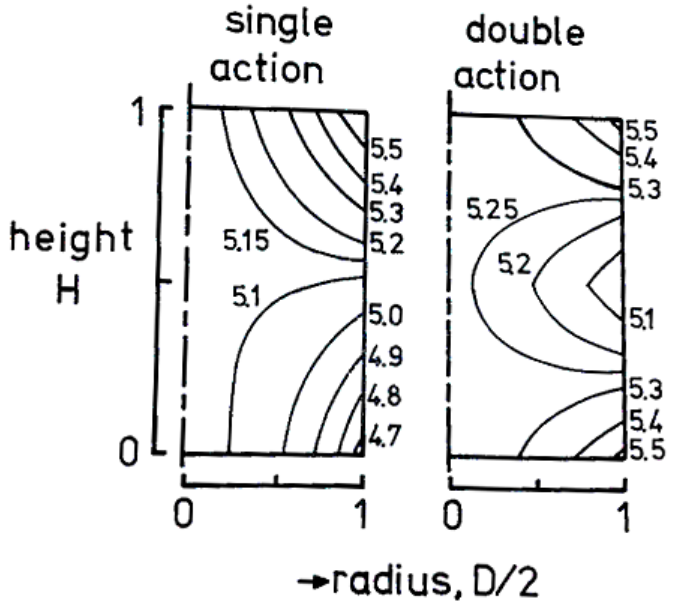

Figure 5: Isodensity (g/cm^3) lines in copper powder for single and double action uniaxial pressing [2]

As can be seen from Figure 5 above, although double action uniaxial pressing reduces the density disparity, there is still a density gradient present. This is magnified for parts with complex shapes, undercuts or large length-to-diameter ratios. One alternative used to reduce these disparities is Cold Isostatic Pressing (CIP). In this technique, a flexible mould is filled with the mixed powder and introduced into a container containing a non-compressible fluid such as oil or water. The container is then pressurized, achieving consolidation. The use of a rubber mould allows the use of complex shapes, but its dimensions must be designed oversize to allow for the compaction shrinkage. A typical schematic of a typical CIP is shown in Figure 6 below. It should be noted that when compared with uniaxial pressing, the CIP technique shows increased density for a given pressure, but with significantly increased cost and decreased throughput. [2]p137

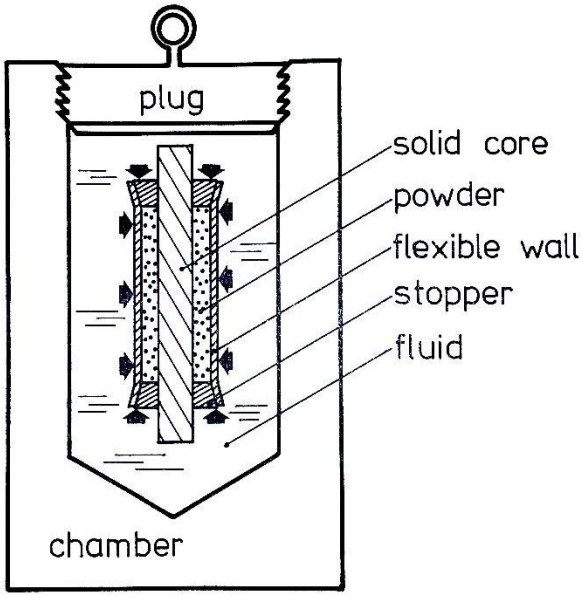

Figure 6: Typical wet-bag cold isostatic pressing, showing pressing of a tube [2]

Hot Isostatic Pressing (HIP) is similar to CIP in that the powder is put into a flexible container and put in a pressurized chamber, but in the case of HIP the sintering procedure is performed while the powder is under isostatic pressure. As seen in Figure 7 below, this allows the HIP process to achieve higher densities. However, this combination of high pressures and temperatures introduces additional complexities and significant additional cost, especially when used to produce alloys designed for high-temperature use.

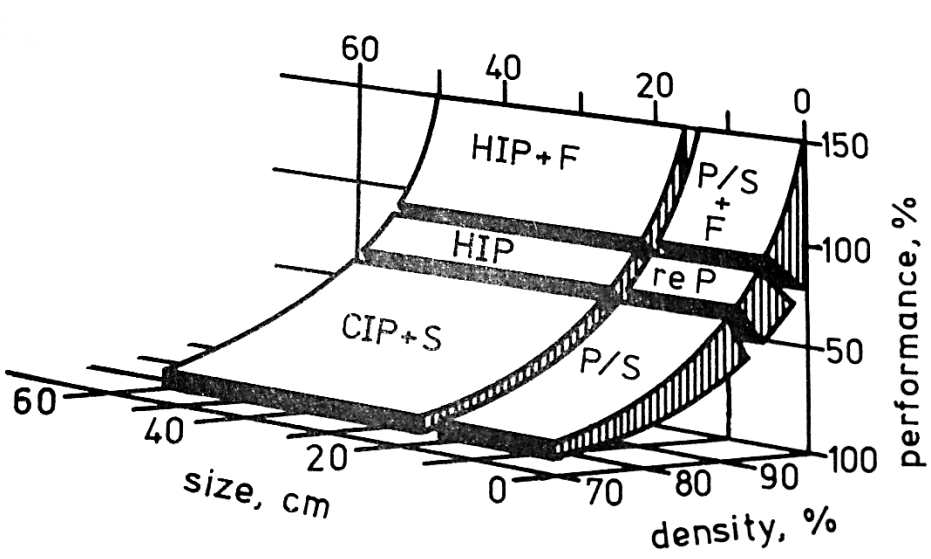

Figure 7: Size, density, and performance of PM parts, and their associated processes [2]

2.1.4. Sintering

Following the creation of the fragile green bodies, a sintering operation must be performed to create a part with much greater properties than its green counterpart. Two important sintering types are solid-state sintering, and liquid phase sintering.

2.1.4.1. Solid State Sintering

In solid state sintering, the powder particles remain in the solid state as would be expected from the name, remaining below the solidus temperature of the alloy system. In this process, adjacent particles contact each other and form a neck, reducing both the surface energy of the

particles and the free energy in the system. Figure 8 below shows a micrograph of the necking process, and Figure 9 below shows the stages of this process between two powder particles. [2]

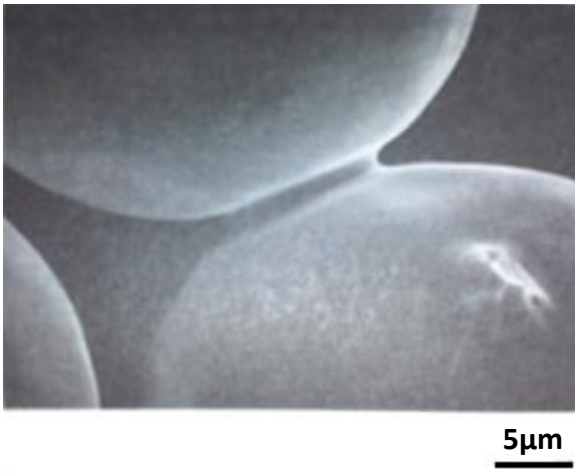

Figure 8: Micrograph of interparticle neck formation [2]

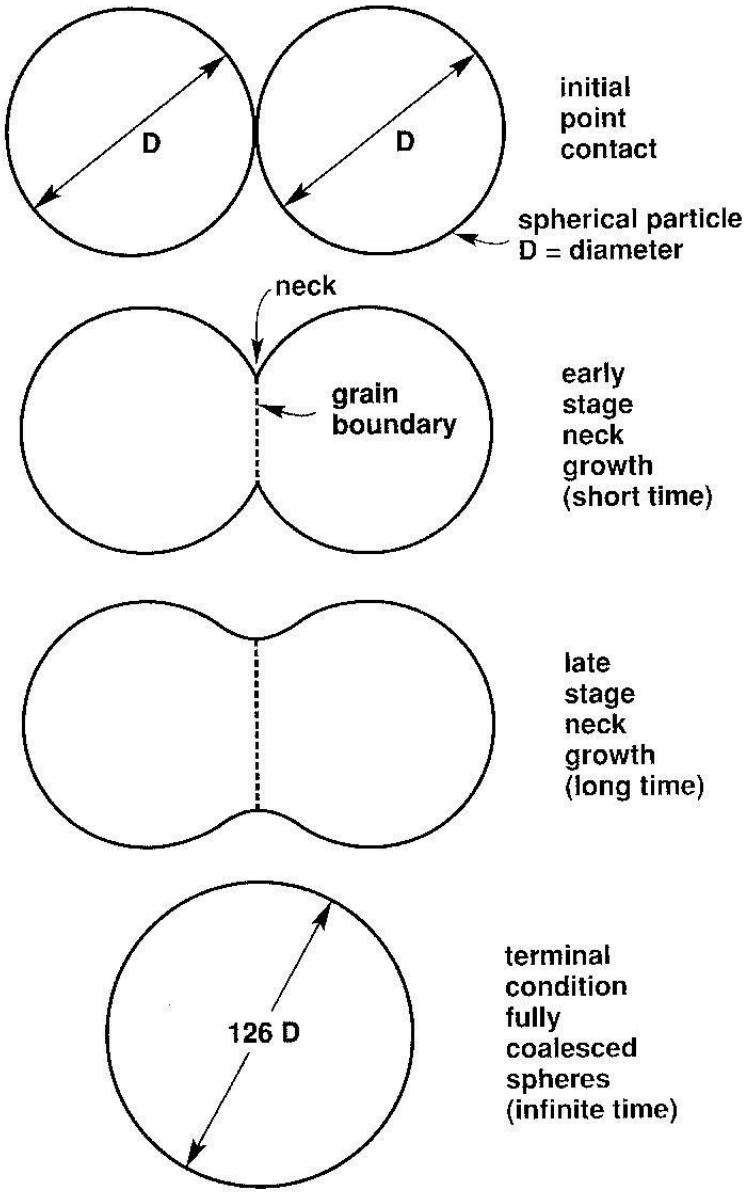

Figure 9: Solid state sintering between two powder particles [6]

Two primary transport mechanisms occur to create the neck growth in the process shown in Figure 9 above: surface transport, and bulk transport mechanisms. They are shown in Figure 10 below. Surface transport is effected by three processes: evaporation-condensation (EC), volume

diffusion (VD) and surface diffusion (SD). Bulk transport, on the other hand, is caused primarily by grain boundary diffusion (GB) and volume diffusion (VD).

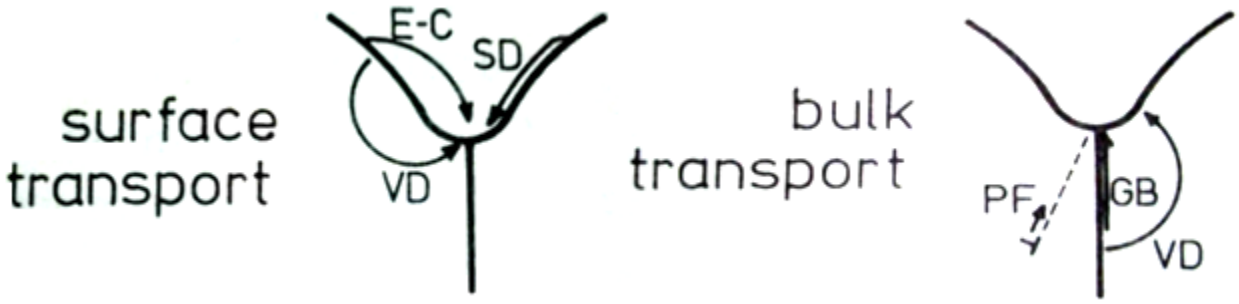

Figure 10: Diagram of surface and bulk transport mechanisms [2]

2.1.4.2. Liquid Phase Sintering

In the case of alloys created using powders with significantly different melting points, some powder particles may melt below the overall sintering temperature, leading to liquid phase sintering. This technique has the advantage that the liquid phase (composed of the powder elements with lower melting points) can spread through the porous structure of the green compact, being drawn in by capillary action. This has the potential to increase the density of the sintered material. Three main conditions must be achieved for a successful liquid-phase sintering to occur: high solubility of the solids in the liquid, low solubility of the liquid in the solids, and wetting of the solid powder particles by the liquid. The material passes through four key stages: particle heating, particle rearrangement, solution-reprecipitation, and finally solid state sintering. These stages are shown in Figure 11 below.

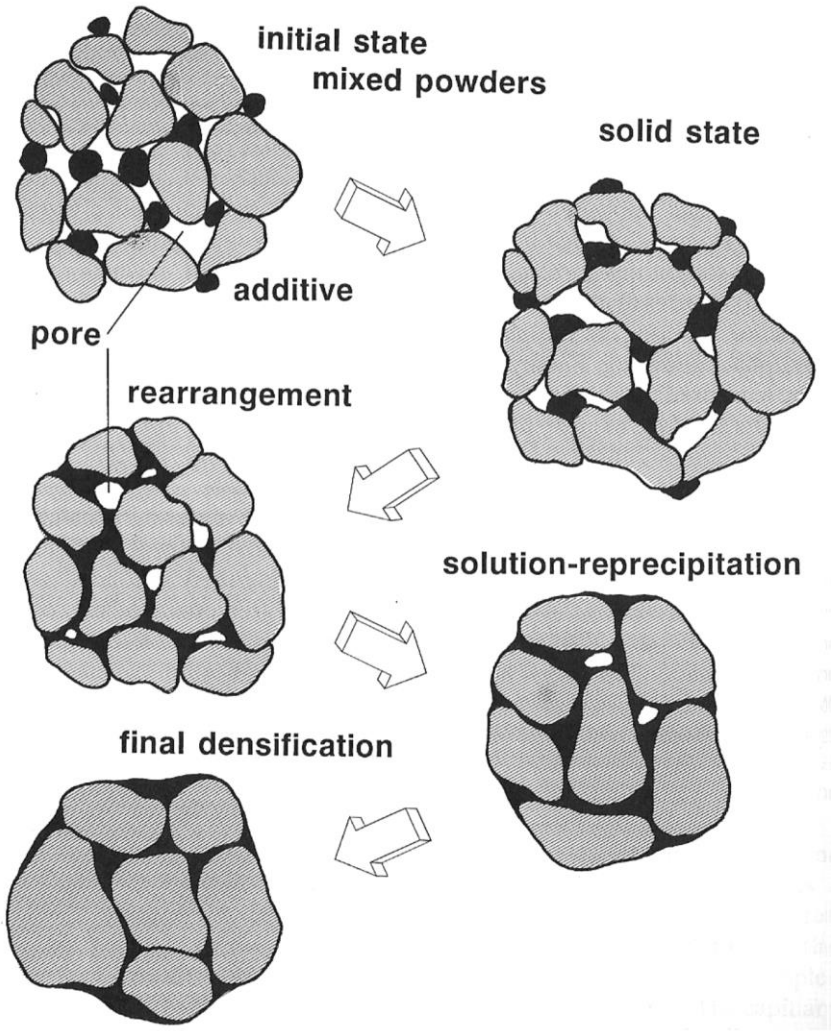

Figure 11: Stages of liquid-phase sintering [6]

Liquid phase sintering is used in this thesis, as the aluminium component of the alloy (added to allow the formation of Gamma Prime precipitates) melts at a much lower temperature than the final sintering temperature of 1300°C, and reacts with the surrounding ternary master alloy powder particles.

2.2. Superalloys

Superalloys have changed significantly since their inception during the military development of the 1940s. They have gained a more refined microstructure, increased physical properties, and have continued to be improved upon. Figure 12 below shows amongst other things the refinement of grain boundaries, and greatly increase precipitate volume fraction through their first 30 years of use.

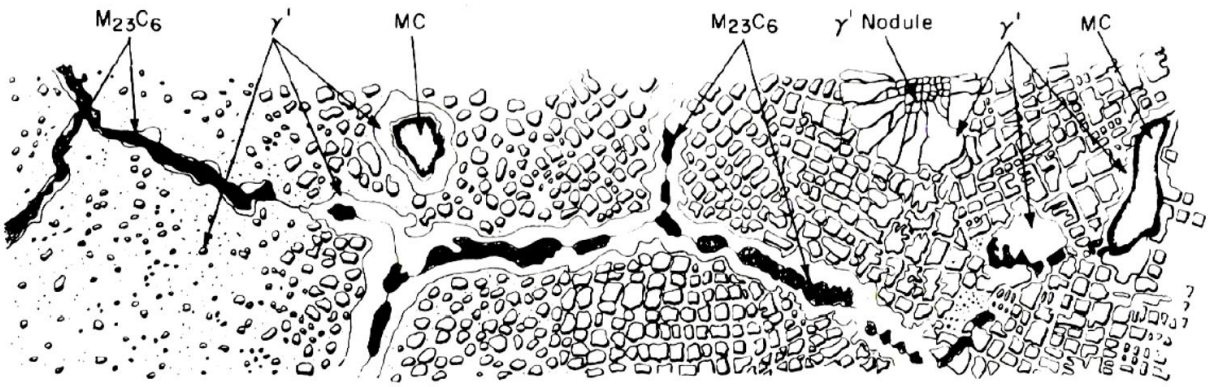

Figure 12: Microstructure progression of nickel-based superalloys from 1940 to 1970 [3]

2.2.1. Alloying Elements

Nickel-based superalloys derive their superior properties from their relatively high alloy content, which allows the formation of high volume fractions of precipitates, enables their high-

temperature creep resistance and protects the alloy from corrosion. Table 1 below contains the most often used alloying elements as well as their contributions to the nickel-base superalloys.

Table 1: Common Alloying Elements in Ni-Base Superalloys [7] [8]

Element	Known Effect
Cr	Oxidation resistance, carbide former ($M_{23}C_6$ and M_7C_3)
Mo, W	Solid-solution strengthening, carbide formers (M_6C and MC)
Al, Ti	Formation of Gamma Prime hardening precipitate, Ti forms MC
Co	Raises solvus temperature of Gamma Prime
B, Zr	Increases rupture strength, B forms borides when present in large quantities
C	Formation of various carbides (MC, M_6C, $M_{23}C_7$, M_7C_3)
Nb	Formation of Ni_3Nb hardening precipitate, carbide former
Ta	Solid-solution strengthener, carbide former (MC), formation of Gamma Prime

2.2.2. Major Microstructural Components in Ni-based Superalloys

In modern nickel-base superalloys, several phases are present; some of the major ones are the Gamma matrix (γ), Gamma Prime precipitates (γ'), various carbides, and topologically close-packed phases. Most relevant to this thesis are the Gamma matrix and Gamma Prime precipitates.

2.2.2.1. Gamma

The matrix of nickel-base superalloys is an austenitic phase with a disordered Face Centered Cubic (FCC) structure. This phase is instrumental in enabling Ni-base superalloys to be used at high service temperatures (up to $0.9T_m$). This is due to three main reasons [3] p101-102:

- Nickel can easily tolerate alloying elements without phase instability due to the nearly-filled 3rd electron shell.
- If chromium is added, the alloys tend to form Cr_2O_3-rich scales with low cation content, which protect the alloys by reducing the inward diffusion of aggressive atmospheric elements (such as oxygen, nitrogen and sulfur) as well as by reducing the outward diffusion of metallic elements.
- At higher temperatures, the alloys tend to form Al_2O_3-rich scales that are exceptionally resistant to oxidation.

The Gamma matrix can be seen in Figure 13 and Figure 14 below, along with embedded precipitates. The Gamma matrix is the lighter-coloured material.

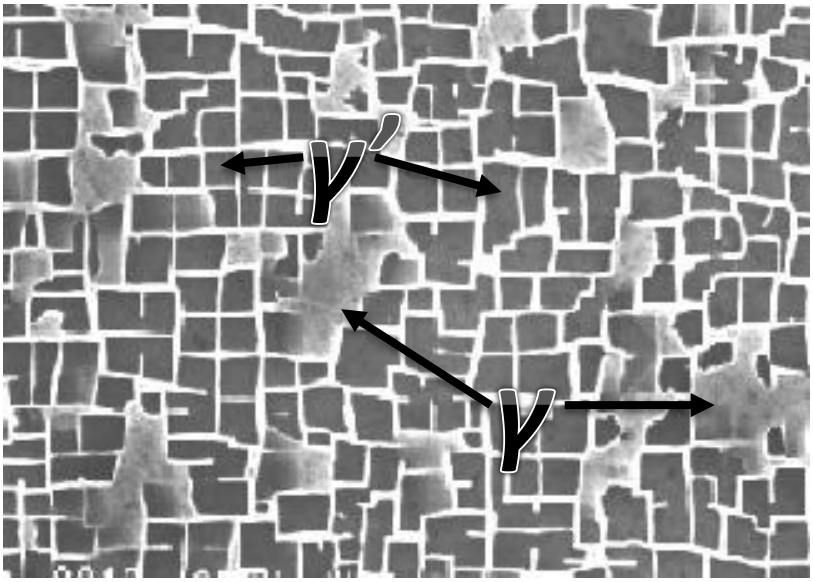

Figure 13: Image of a Ni-based Superalloy Showing Clear γ' Precipitates and γ Matrix [8]

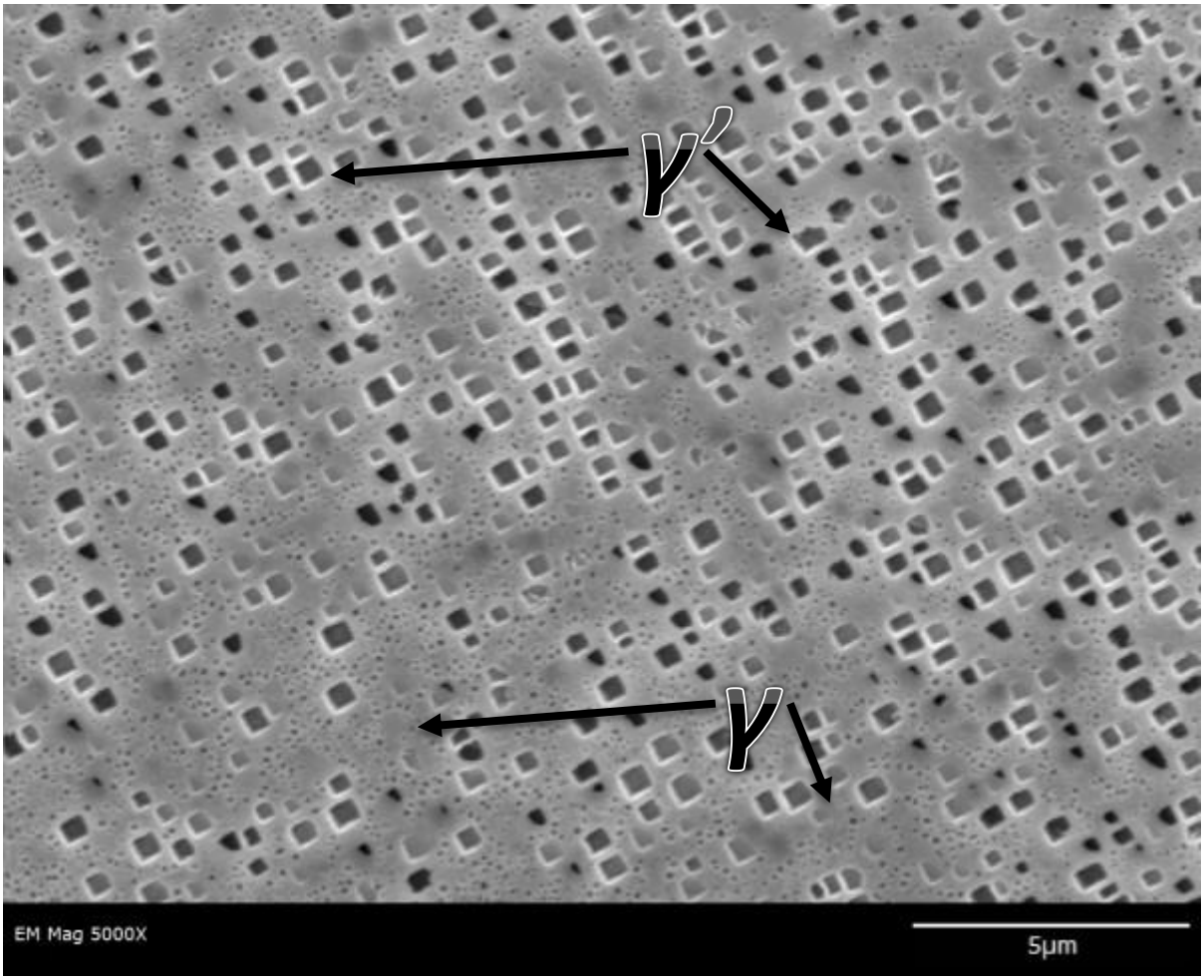

Figure 14: Image of Gamma matrix with Primary and Secondary populations of Gamma Prime Precipitates [9]

2.2.2.2. Gamma Prime

This phase is an ordered FCC compound of A_3B form, most often of the form $Ni_3(Al/Ti)$. The Gamma Prime phase contributes significant strength to nickel-based superalloys by hindering dislocation motion. In addition, Gamma Prime is ductile enough to avoid being a source of

fracture, unlike the severe embrittlement caused by the Sigma precipitates discussed in Section 2.2.2.4 below. [3] (p104-5)

Gamma Prime precipitates can be seen in Figure 13 and Figure 14 above, including a secondary (smaller) population of Gamma Prime in Figure 14. The Gamma Prime is the darker shapes, with the primary Gamma Prime appearing as cubic shapes, while the secondary population can be seen as darker dots in the matrix.

As can be seen in Figure 15 below, Gamma Prime has a rather narrow composition range, centered on 86.4% Ni by weight.

Al-Ni

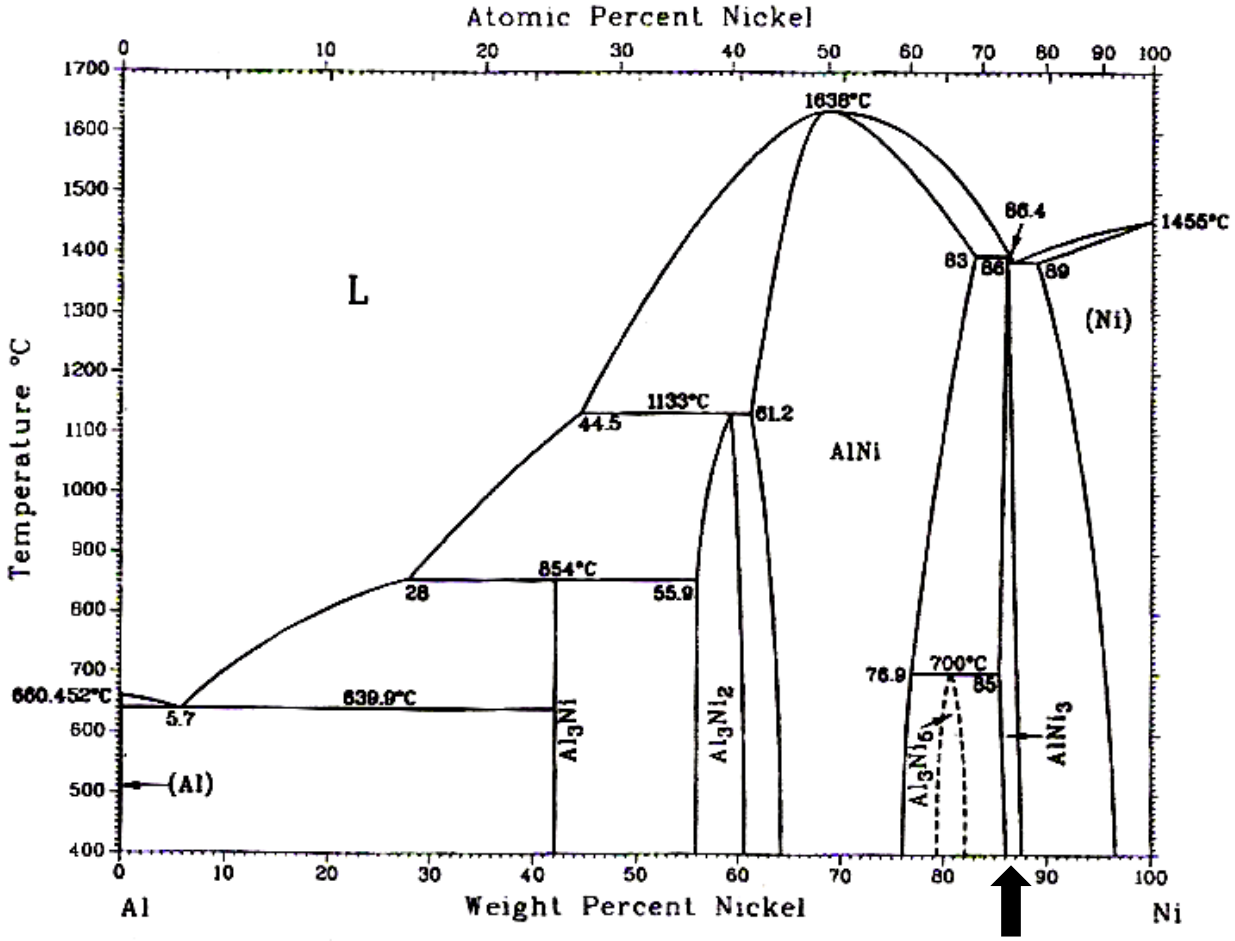

Figure 15: Al-Ni Binary Phase Diagram [10]

Interestingly, the yield strength of the Gamma Prime phase increases as temperature increases reversibly between -196°C and 800°C. The degree of this increase is strongly dependent on the exact aluminium content in the Gamma Prime phase. When exposed to temperature above $0.6T_M$, the Gamma Prime precipitates ripen (grow) at a significant rate, which facilitates dislocation bypassing. [3] (p109)

Section 2.4 gives a discussion of the precipitation of the Gamma Prime phase from the Gamma matrix.

The Gamma Prime phase also keeps its long-range order to near its melting point (1385°C). As it is an ordered substitutional solid solution (see Section 2.2.3.2 below for more information), Gamma Prime has a limited range of compositions, but alloying elements may substitute for each other significantly. Specifically, in most nickel-base alloys, up to 60% of the Gamma Prime's aluminium can be replaced by titanium or niobium. [3] (67)

2.2.2.3. Carbides

Although intragranular carbides are common in iron- and cobalt-based superalloys, in nickel-based superalloys carbides appear primarily at grain-boundaries. Although certain grain-boundary carbides reduce ductility, carbides can also increase creep life and rupture strength at high temperatures. Carbides can also influence the stability of the matrix by removing reacting elements such as Cr, Mo, and W. The addition of carbon (and thus carbides) depends heavily on the precise composition and service conditions of the alloy. The most common carbides in nickel-based superalloys are shown in Table 2 below. [3]

Table 2: Common Carbides in Ni-Superalloys [3]

Carbide	Characteristics
MC	Usually found as coarse random cubic or script precipitates. Usually forms during solidification, distributed heterogeneously. They have an FCC structure
$M_{23}C_6$	Prefers grain boundaries; usually found as irregular blocky particles (plates and regular geometries have been observed). Profuse in alloys with moderate/high chromium content. They form at lower temperatures (760-980°C) from decomposition of MC carbides and carbon solute in the matrix. Can increase rupture strength by inhibition of grain boundary sliding
M_6C	Present in blocky form at grain boundaries, more rarely in a Widmanstätten pattern. Form at 815-980°C

2.2.2.4. Topologically Close-Packed Phases

Topologically Close Packed (TCP) phases are generally detrimental phases that tend to appear as thin linear plates or needles. They can also be present with a "basket-weave" morphology, which consists of ribbons of precipitates overlapping at right angles. TCP phases tend to precipitate on grain-boundary carbides. The crystal structure consists of closely packed layers of smaller atoms (such as nickel and chromium), with larger atoms residing in sites between the layers. These layers are aligned with the octahedral planes of FCC crystals. In nickel-based alloys, the TCP phases are: σ (rich in Cr and low in Mo), μ (rich in Mo or W), as well as R and P

(both having roughly equal ratios of Cr and Mo). Interestingly, multiple TCP phases may be present in the same precipitate. [11] [3] (p112-115)

Undesirable effects of TCP include damage accumulation or cracking due to brittleness, softening of matrix due to depletion of strengthening elements [12]

2.2.3. Strengthening Mechanisms in Ni-based Superalloys

Strengthening mechanisms for an alloy system must be well understood, both to adjust the alloy's properties for their service conditions, and to enable various processing procedures. The strength of a material is determined by its ability to resist the movement of dislocations, and therefore all strengthening mechanisms impede this movement in one way or another. For nickel-base superalloys, three primary hardening mechanisms must be taken into account: strain hardening, solid solution strengthening, and precipitation strengthening.

2.2.3.1. Strain Hardening

Strain hardening (also called work hardening) occurs when a material is plastically deformed at low temperatures relative to their melting point. Dislocations are created and move as the

material deforms. As more and more dislocations are present in the deformed area, they impede one another's movement as would multiple wrinkles in a carpet. Figure 16 below shows the changing yield strengths of 1040 steel, brass, and copper, as they are deformed and the dislocations accumulate.

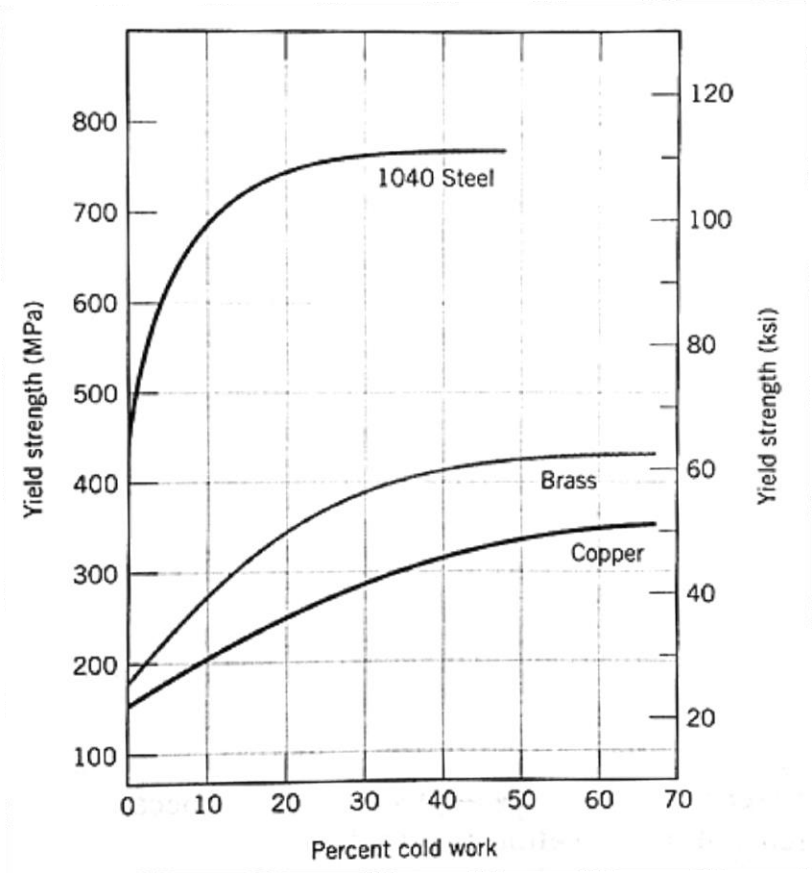

Figure 16: Increase in yield strength of selected materials with percent cold work [13]

2.2.3.2. Solid Solution Strengthening

General theory of Solid Solution Strengthening

Early humans discovered five thousand years ago that, by creating a mixture of tin and copper, they could obtain a material tougher and stronger than they previously had, leading to the dawn of metallurgy, the Bronze Age, and the beginning of urban civilization. Solid solution strengthening is achieved by dissolving one metal into another. Depending on the relative size of the alloying and base elements, two types of solid solutions can occur. If the solute atoms are of similar or greater size, they are substituted for the solvent atoms in the crystal lattice (as illustrated in Figure 17 below), creating a substitutional solid solution. [14]

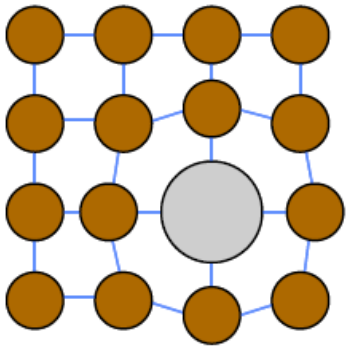

Figure 17: Representation of a substitutional solid solution [14]

If the solute atoms are of sufficiently smaller atomic radii, such as in the case of carbon in iron, they may fit into the interstices between the solvent atoms (as shown in Figure 18 below), creating an interstitial solid solution.

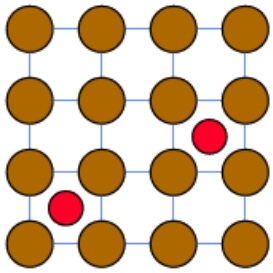

Figure 18: Representation of an interstitial solution [14]

The substitutional or interstitial atoms result in distortions in the crystal lattice and act as "roadblocks" that can significantly impede the movement of dislocations. This is illustrated in Figure 19 below. [14]

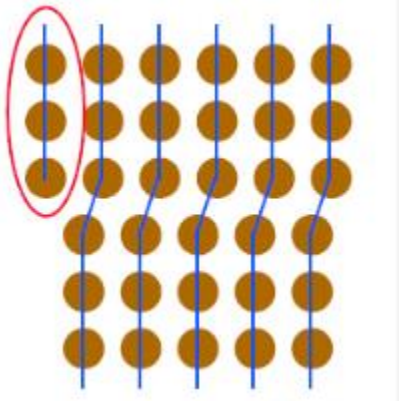

a) Introduction of a dislocation

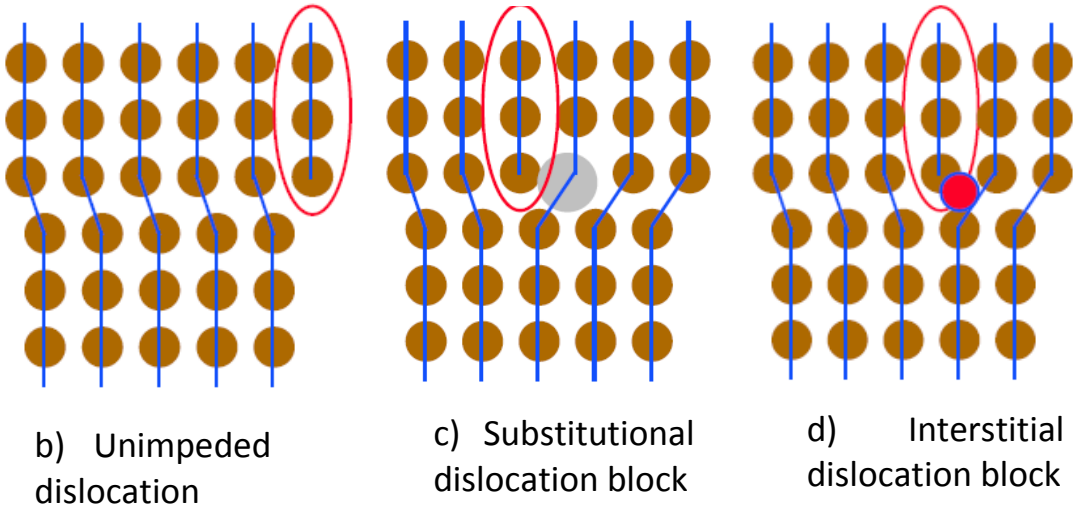

Figure 19: Behaviour of dislocations in unalloyed material and solution strengthened materials [14]

Effect of solution strengthening in nickel-base superalloys

In the case of precipitation-hardening nickel superalloys, the effect of solid solution strengthening is most felt in the Gamma phase matrix. Common alloying elements for these alloy systems are cobalt, iron, chromium, molybdenum, tungsten, titanium and aluminium [3] (p63), with atomic diameters being oversize from nickel by a factor ranging from 1% (for cobalt) to 13% (for tungsten). The hardening effect of elemental additions can be correlated to atomic diameter oversize by measuring lattice expansion, to the point of being able to estimate an alloying element's contribution to hardening by calculating its effect on lattice constants. Interestingly, aluminium, often thought of only as a precipitation strengthener (forming Gamma Prime precipitates), is also a strong solid-solution strengthener, with tungsten, molybdenum and chromium being strong contributors as well. On the other hand, iron, titanium, cobalt and vanadium have a significantly weaker effect. At temperatures above $0.6T_M$ (such as for turbine use), high-temperature creep is in effect and the strength of the Gamma phase is related to its

resistance to elemental diffusion. As such, molybdenum and tungsten are potent hardeners at those temperatures, given their resistance to diffusion. [3] p102-104

2.2.3.3. Precipitation Hardening

Second-phase particles, also known as precipitates, can be introduced to alloys to strengthen and toughen them. This section discusses the concept of precipitate strengthening in general, as well as some of their effects in nickel-base superalloys specifically.

General theory of precipitation hardening

As in solid solution strengthening, precipitation strengthening is achieved by introducing obstacles to dislocation motion. As a dislocation line travels through a material, it encounters precipitates. This causes the dislocation line to bow around the precipitates, exerting a force on them as shown in Figure 20 below. [15]

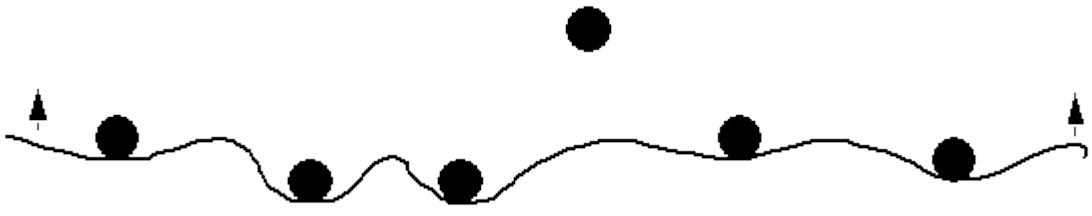

Figure 20: Dislocation line encountering precipitates [15]

For the material to continue deforming, the dislocation line must somehow pass the precipitates. It can do this in one of two ways: by cutting entirely through the precipitates (Figure 21), or by curving around each particle to form an Orowan loop (Figure 22).

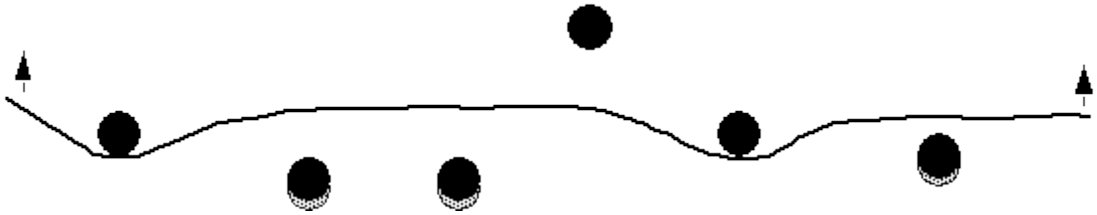

Figure 21: Dislocation line cutting precipitates [15]

For precipitate cutting to occur, the critical stress is determined by:

$$\tau_c = \frac{F_c^{\frac{3}{2}}}{b^2 l_o \sqrt{G}} \qquad \textit{Equation 1}$$

Where F_c is:

$$F_c = \frac{2Tl_o^2}{\lambda^2} \qquad \textit{Equation 2}$$

And where T is line tension and can be represented as $0.5Gb^2$; and λ is the mean interparticle distance along the dislocation line; *G* is the shear modulus of the matrix; *b* is the Burgers vector of the dislocation; and l_o is the average interparticle spacing. [15]

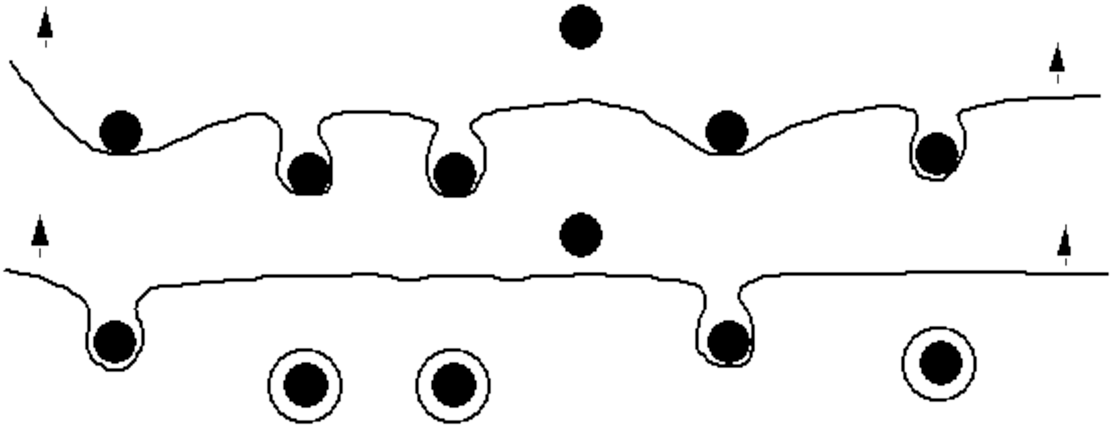

Figure 22: Dislocation line undergoing Orowan looping [15]

In the case of Orowan looping, the critical stress for the looping to occur is:

$$\tau_c \sim \frac{Gb}{l_o} \qquad \textit{Equation 3}$$

By plotting the critical stress equations, we can obtain Figure 23 below

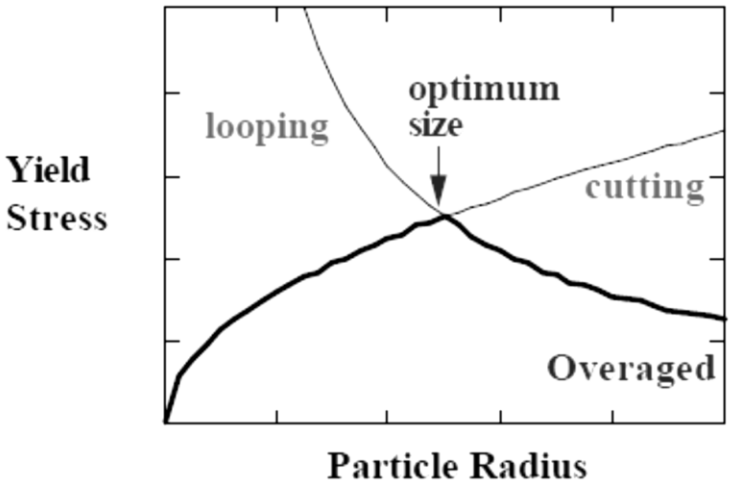

Figure 23: Plot of critical stresses of cutting and Orowan looping [15]

From this plot, it is possible to infer that smaller particles will fail by cutting, while larger ones will be subjected to Orowan looping. As can be seen from Figure 23 above, there is also a peak in the stress required for failure. This indicates the precipitates' optimal size, and emphasizes the need to be able to predict and control precipitate size.

Effect of precipitation strengthening in nickel-base superalloys

Nickel-base superalloys derive their superior strength from the presence of coherent and stable intermetallic precipitates such as Gamma Prime [Ni_3(Al,Ti)] and Gamma Double Prime [Ni_3(Cb,Al,Ti)]. Other phases, such as carbides or borides have minimal effect on the strength of the alloy, although they may have more influence on creep rate and other related properties. [3] (p66)

Research by Murray has shown that the alloy system used in this thesis undergoes an increase in hardness of approximately 40% when 6% Al was added as a precipitate former to the base Ni-Cr-Fe ternary alloy. [16]

2.3. Microscopy Techniques

The ability to document the changes to a material at the microstructural level is essential to fully understanding the characteristics of a material subjected to various conditions. Information on the elemental distribution, the microstructure and the macrostructure (such as pores) can be essential to determining when and why some changes occur. Some of the best tools for obtaining this information are Electron Microscopes (both Scanning and Transmission) as well as the Atomic Force Microscope.

2.3.1. Electron Microscopy

The defining characteristic of electron microscopy is the fact that the sample is impacted by a primary electron beam. Common electron microscopes generally fall under one of two types: the Scanning Electron Microscope (SEM) and the Transmission Electron Microscope (TEM). In the case of the SEM, the products of the interaction between the primary electron beam and the sample are then detected and analyzed. In a TEM, as the name implies, the detector is positioned such that it intercepts the electrons transmitted through the sample.

2.3.1.1. Scanning Electron Microscope

The Scanning Electron Microscope can easily create images that can be surprisingly easily interpreted by even laymen unfamiliar with the equipment. In an SEM, an electron beam is produced (by heated filament or other method) and passed through magnetic lenses to condense and focus the beam. The electron beam then enters the sample chamber and strikes the samples, giving off various types of photons and electrons, which can then be captured by their respective detectors. One of the strengths of the SEM is that its rastering beam can provide near-real-time images, allowing rapid exploration of the samples that are to be examined. A schematic of a typical SEM using a secondary electron detector is shown in Figure 24 below. [17]

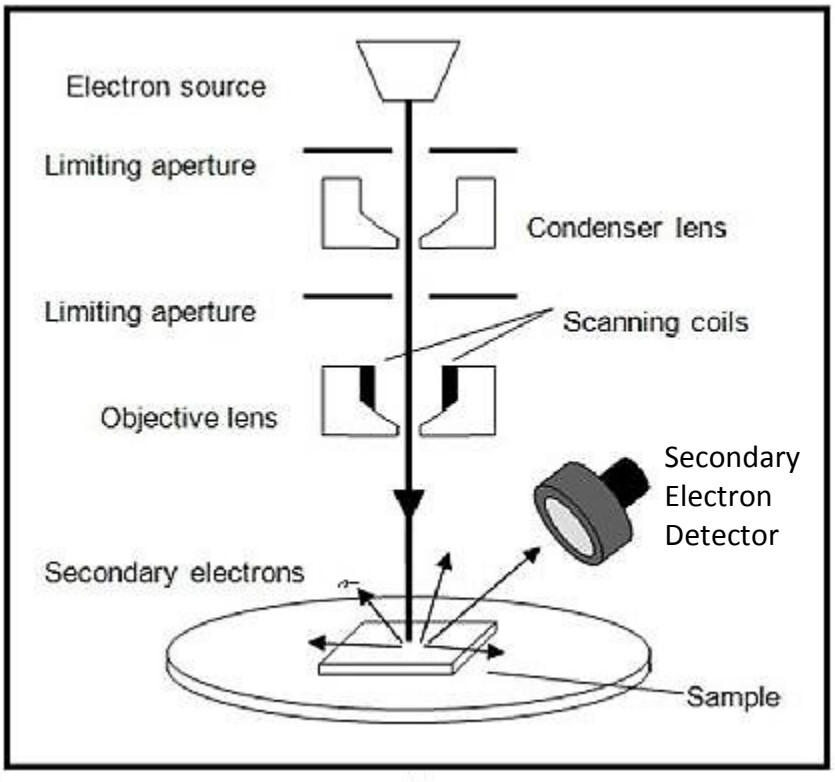

Figure 24: Schematic of typical scanning electron microscope [18]

The two primary detectors used to obtain images from an SEM are Secondary Electrons (SE) and Backscattered Electrons (BSE)

SE images are obtained from electrons that are ejected from the specimen's atom's shells by *inelastic* scattering interactions (some energy transfer to sample), also known as plasmon production. As the incidence angle of the primary electron beam is decreased, the escape distance will decrease on one side of the interaction volume, enabling more secondary electrons to escape from that area. Because of this, angled surfaces and edges are brighter than flat surfaces, making the SE imaging mode well-suited to topographical images. [17]

Backscattered electron images are obtained from electrons that originate in the primary electron beam, and are back-scattered out of the specimen by *elastic* scattering interactions (kinetic energy essentially remains constant) with the specimen's atoms. Because of their higher number of protons (and associated electrons), atoms with a higher atomic number produce backscatter electrons more strongly than those with lower atomic numbers. This causes compounds with a higher average atomic number to appear brighter in a BSE image, while compounds with lower average atomic numbers appear darker. This mode is particularly useful when working with chemically dissimilar compounds, as it can provide high contrast as well as indications as to the atomic constituents of the phases. [17]

Figure 25 below shows the most commonly used interaction products as well as their relative interaction volumes.

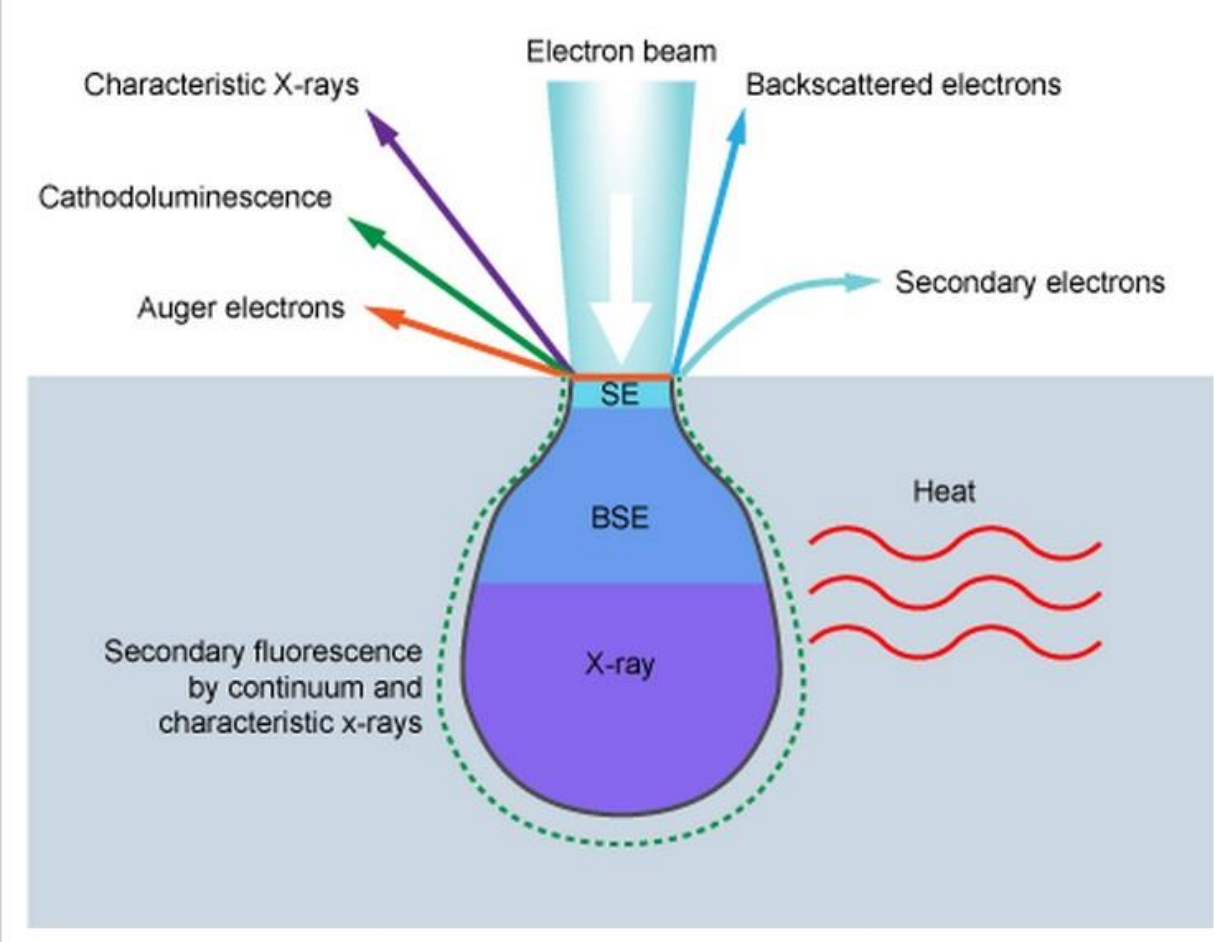

Figure 25: Schematic diagram of primary electron beam interaction products and respective volumes [19]

Another result of the electron beam interaction with the sample is the production of "characteristic X-rays". Characteristic X-rays are X-ray emission spectra unique to a certain element's electron configuration (as separate from continuum X-rays). The energy from the

primary electron beam provides enough energy for some electrons to be ejected from their atoms' shells. An electron located at a higher energy state then drops down to fill the vacancy caused by the ejected electron. This transition from a higher energy state to a lower one releases photons (radiation energy) of a specific wavelength, which is determined by the energy difference between the two levels. This process is illustrated in Figure 26 below [17]

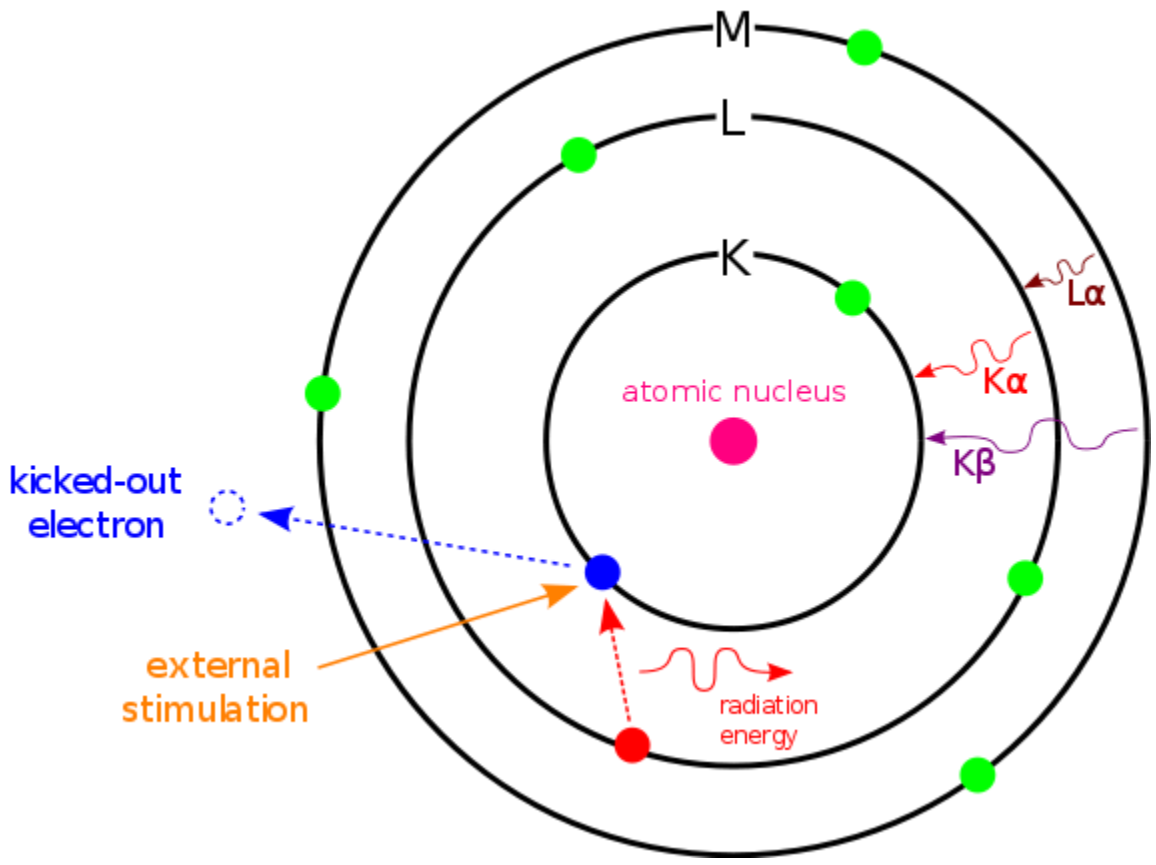

Figure 26: Illustration of characteristic X-ray production process and nomenclature [20]

As elements have characteristic electron shell energies, the electron drops create characteristic X-rays. For a naming convention, an electron dropping one energy level to a K-shell is called a

Kα transition, while a two-level drop to a K-shell is called a "Kβ" transition. Similarly, a single-level drop to an L-shell is called an "Lα" transition, and so on.

Characteristic X-rays can be used to determine the composition of the sample, and even obtain elemental distribution maps. The two main methods of analysis are energy dispersive spectrometry (EDS) and wavelength dispersive spectrometry (WDS).

2.3.1.2. Transmission Electron Microscope

Where the scanning electron microscope detects electrons produced by the impact of the primary electron beam onto a sample, the transmission electron microscope detects electrons that were *not* intercepted by a thin film of the sample. [21]

The primary advantage of the TEM is its ability to achieve a significantly higher resolution that the SEM: details can be resolved to 0.2nm. [22]

One significant downside of the TEM method is the need for extensive preparation to obtain intact thin sections. Specimens must be thinned to such a degree that they are transparent to electrons; that is, to transmit sufficient electrons through to the detector. In the case of a TEM

using 100kV electrons, aluminium alloys would be sufficiently thin up to approx. 1µm, whereas steels would be sufficiently thin up to several hundred nanometers. Furthermore, a TEM almost always produces better results with thinner specimens, such that specimen thicknesses of less than 100nm are desirable. To achieve this, specialized is equipment is required. One such apparatus, the focused ion beam, costs approximately as much as a TEM. Depending on the specimen preparation method chosen, preparation of a single specimen can take up to 2 days. Another potential disadvantage of the TEM (which is also present in high-magnification SEMs) is the possible modification of the sample by the high-energy beam of electrons. [21]

2.3.2. Atomic Force Microscope

The Atomic Force Microscope (AFM) is a relatively recent development in the field of small-scale imaging. It was first constructed as a further development of the Scanning Tunnelling Microscope in the mid-eighties. [23]

As the AFM depends on a physical nanoscale tip instead of photon or electron optics, it has significantly higher resolution, allowing easier imaging of features that were previously the province of preparation-intensive TEM microscopes. [23]

The principles behind atomic force microscopes are relatively simple, as shown in Figure 27 below. A laser impinges on the cantilever surface and is reflected to a photodetector, and the resulting deflection data are used to regulate piezoelectric actuators which control the location of the cantilever probe.

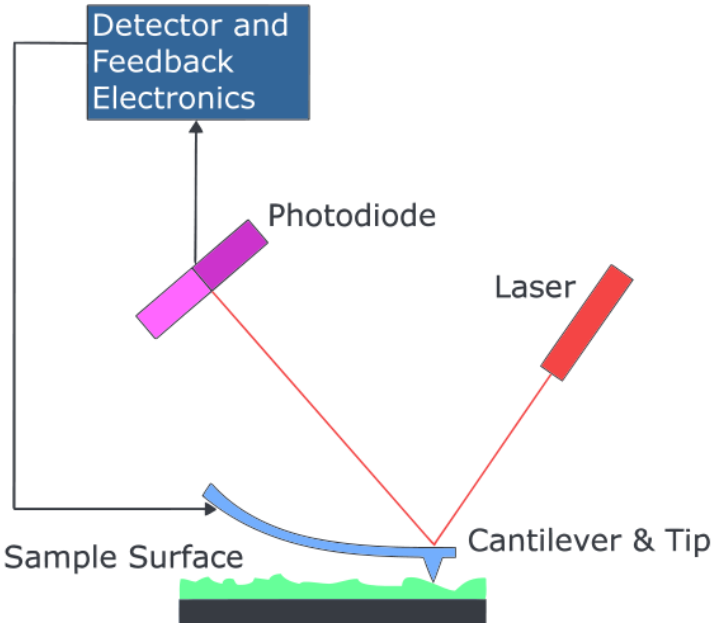

Figure 27: Schematic of AFM control system [24]

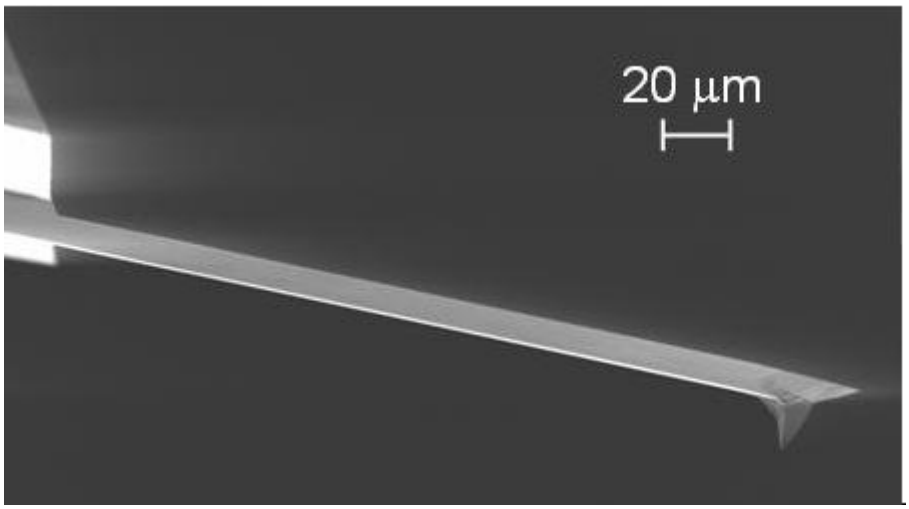

Figure 28: AFM Cantilever, with nanoscale tip (lower right) used to contact surface [25]

Three main methods can be used to obtain surface topography data with an AFM: Contact mode, Tapping mode, and Non-Contact mode.

In **Contact mode**, the probe tip is dragged across the sample surface, and the deflection data recorded and used to create a topographical map of the sample. As other forces may affect the cantilever deflection, a slight force is applied to the cantilever to ensure that the tip is pressed against the sample such that the applied forces from this surface are repulsive. This force is kept near-constant by maintaining a set deflection. Using contact mode may damage softer samples, and even harder ones with repeated scanning. [23]

Tapping mode is used to image softer samples. In this method, the cantilever is driven to oscillate at a frequency near (typically 2% offset) to its resonant frequency. The probe tip is then brought into contact with the surface at the bottom of its oscillation. The forces acting on the cantilever then retard the phase, data which is used to maintain a set oscillation amplitude as well as to create a topographical map. The record of the phase-offset data can also indicate variations in sample stiffness and hardness. [23]

This mode is particularly useful to image non-homogeneous materials such as powder-metallurgy alloys, as it avoids dragging the imaging tip across discontinuous features, and damaging either the tip, or the features.

In **Non-Contact mode**, a two-stage raster is used. On the first pass, a topographical map is obtained by tapping. This raster is then re-traced with the cantilever a set distance above the surface. Depending on the material and coating of the cantilever and tip, various non-contact forces can then be measured from the deflection, such as electric or magnetic forces. This is especially useful for the measurement of micro- or nano-scale circuits, as it is possible to measure current due to the formation of electric and magnetic fields. [23]

Some of the advantages of the AFM over the TEM are reduced preparation time (as the specimen does not need to be reduced to a thin film), as well as the ability to obtain topographical data (the TEM can only image cross-sectioned samples). [26]

2.4. Precipitation and Growth of Gamma Prime

The precipitation of Gamma Prime from the Gamma matrix is extremely rapid. According to Sims et al [3] (p104), the compatibility of Gamma Prime with Gamma, both being FCC crystal

structures and having similar lattice constants (approx. 0.1% mismatch), allow homogeneous nucleation of the Gamma Prime phase with low surface energy and high long-time stability.

Furzman et al. [27] experimented with various cooling rates to optimize the volume fraction of Gamma Prime to improve creep resistance- a cooling rate of 287°C/min was found to give a volume fraction of 40%.

In “Progress in Ostwald ripening theories and their applications to the γ’-precipitates in nickel-base superalloys” [28], A. Baldan examined various different methods and models to predict the size and distribution of Gamma Prime precipitates. Regardless of the exact method used, a cubic particle growth relationship was found to be accurate.

2.5. Past Work on Similar Alloys

The alloy used in this thesis (see Section 4.1 for details) is similar in composition to Inconel 600, but with added aluminium and silicon. Work has been done on this alloy system previously by Akinlade et al., and Murray et al.

Akinlade et al. focused primarily on developing processing methods suitable for this alloy system [29]. Murray et al, in turn examined the influence of minor elemental addition of Si and

Y on the PM alloy's oxidation resistance. As one of the issues with powder metallurgy is the propensity of parts to retain porosity post-sintering, Murray attempted to reduce the porosity using a thermo-mechanical deformation process, heating the samples to 1200°C and compressing samples by up to 30% using a Gleeble thermomechanical test unit. Following this process, Gamma Prime precipitates were not visible using a Scanning Electron Microscope, leading to the conclusion that the Gamma Prime precipitates were solutionized. [5] [16]

However, preliminary experiments lead to the discovery that the thermo-mechanical process used did not change the hardness of the alloys. Therefore, the Gamma Prime precipitates must somehow remain present. An in-depth examination of this phenomenon is given in Section 5.6.

3. Research Objectives

The strength and toughness of alloys containing Gamma Prime precipitates is closely related to both the volume fraction, and the size of these precipitates. The objective of this thesis is to better understand the behaviour of the Gamma Prime phase in a nickel-based powder-metallurgy superalloy similar in composition to Inconel 600. This will allow better control the characteristics of these precipitates, and thus allow optimization of material properties. Samples will be subjected to various heat treatments, as well as high-temperature thermo-mechanical deformation to evaluate techniques for controlling Gamma Prime precipitates. Characterization of the resulting precipitates will be performed using hardness testing, microstructural examination through both Scanning Electron Microscopy (SEM) and Atomic Force Microscopy (AFM), as well as Differential Scanning Calorimetry (DSC).

4. Materials and Methods

This section discusses the alloys used in this thesis, as well as the processing and analytical methods used to examine material samples.

4.1. Materials

Throughout this thesis, samples of the same nominal composition were prepared using two separate powder recipes: master-alloy samples, and elemental-powder samples.

For the master alloy samples, an inert gas atomized ternary alloy powder was used, having a nominal composition of 79% nickel, 12% chromium and 9% iron. The powder was obtained from Alpha Aesar ®, with a 325 mesh size. 6%wt aluminium (from Ecka Granules with a median diameter of 6µm) and 0.5%wt silicon (325 mesh, 99.5% purity) were added to this base powder, giving the composition in Table 3. As the master alloy is a ternary, this composition is referred to through this thesis as “TAS”: Ternary-Aluminium-Silicon.

Table 3: Composition by weight of TAS alloy used in this thesis

	Ni (Wt %)	Cr (Wt %)	Fe (Wt %)	Al (Wt %)	Si (Wt %)
Alloy composition:	73.87	11.22	8.42	6.00	0.50

For the elemental powder samples, the same nominal composition was used, but the various components were introduced as elemental powders. Their respective purity, size and manufacturer are given in Table 4 below.

Table 4: Characteristics of the powders used to create the elemental samples

Elemental Powder	Purity	Median Diameter (μm)	Manufacturer
Ni	99.8%+	63	Alpha Aesar
Cr	99.2%+	<10	Alpha Aesar
Fe	99.5%+	6-10	Alpha Aesar
Al		6	Ecka Granules
Si	99.9985%	37 (325 mesh)	Alpha Aesar

4.2. Powder Processing

4.2.1. Mixing

Mixing of the powders was achieved by blending in a Turbula Model T2M blender for 30 minutes to homogenize the powders.

4.2.2. Compaction

Samples pressed in the uniaxial regime were created as Transverse Rupture Strength (TRS) bars of approximately 31x13x8mm. The compaction was achieved using a Satec Systems Model 5594-200HVL load frame. These bars were pressed at pressures ranging from 200 MPa to 500 MPa. To reduce die wear and improve green density, 0.75% wt of Microwax was added as a lubricant to the mixing process.

Selected samples were also pressed in a CIP to assess the influence of this method on the residual porosity, both as a green compact and as a sintered product. This process was performed in an Avure Technologies LCIP 44260 with a 4in diameter pressure chamber at pressures of 200MPa to 400MPa.

4.2.3. Delubrication and Sintering

Uniaxially-pressed samples (containing Microwax) were delubricated by heating in a Lindberg Blue 3-Zone Furnace Model STF55666C-1. This was performed at 400˚C for 30 minutes in a flowing N_2 atmosphere to vaporize and remove the lubricant.

Sintering was then performed at a vacuum of 10^{-5}torr in a bell furnace from Materials Research Furnaces Inc. The samples were heated at 10˚C per minute; when the samples reached 1300 ˚C the temperature was held for two hours. The samples were then cooled to room temperature at 10 ˚C per minute.

CIP samples were enclosed in Vycor ampoules filled with grade 5.0 argon (medical-grade) at sufficient pressure to bring the ampoule interior to 1atm at the sintering temperature of 1300 ˚C. The ampoules were placed in a Leco SiC muffle furnace at 625 ˚C and heated to 1300 ˚C, where the temperature was held for 2h. The furnace was then turned off, and the samples removed at 700 ˚C.

4.3. JMatPro

JMatPro is a thermodynamic simulation software produced by Sente Software Ltd. which uses the Calculation of Phase Diagram method (CALPHAD) to perform a step-wise equilibrium calculation to minimize Gibbs energy [30].

JMatPro was used as an initial design tool to approximate the phase-change behaviour of the subject alloy upon heating and cooling. This was performed by creating a chart of Phase Content (by weight) vs Temperature (shown in Figure 37), as well as multiple Continuous Cooling Transformation (CCT) curves (shown in Figure 38 and Figure 39) to examine the extent of phase transformations as a function of time for a set cooling rate. Precipitate size estimates were also obtained. JMatPro was used to obtain an estimate for the solutionizing transition temperatures of γ' precipitates.

JMatPro has been used to predict the behaviour of phases present in similar alloy systems [31] [30] [32].

4.4. Differential Scanning Calorimeter

A Netzsch 404C Differential Scanning Calorimeter (DSC) (shown in Figure 29) was used to model the behaviour of the subject alloy from room temperature to 1400˚C. Heating/cooling rates of 5˚C/min were used. Samples were on the order of 50-80mg. The DSC recorded the heat flux to and from the sample, providing information on both the endothermic and exothermic events associated with the intermetallic solutionizing behaviour as well as the melting of the alloy. Using the heat flux curves thus obtained, the solutionizing temperature determined from the JMatPro software could be compared prior to heat treatment of the samples.

Figure 29: Netzsch DSC 404 C Differential Scanning Calorimeter used in this thesis

4.5. Gleeble Thermomechanical Testing

The Gleeble 1500D used in this thesis (shown in Figure 30) is a thermomechanical uniaxial hot-press apparatus that uses resistive heating to achieve temperature control of the sample. The temperature monitoring is performed by a thermocouple welded onto the centreline of the sample, perpendicular to the current flow to avoid temperature-monitoring artifacts from the heating process.

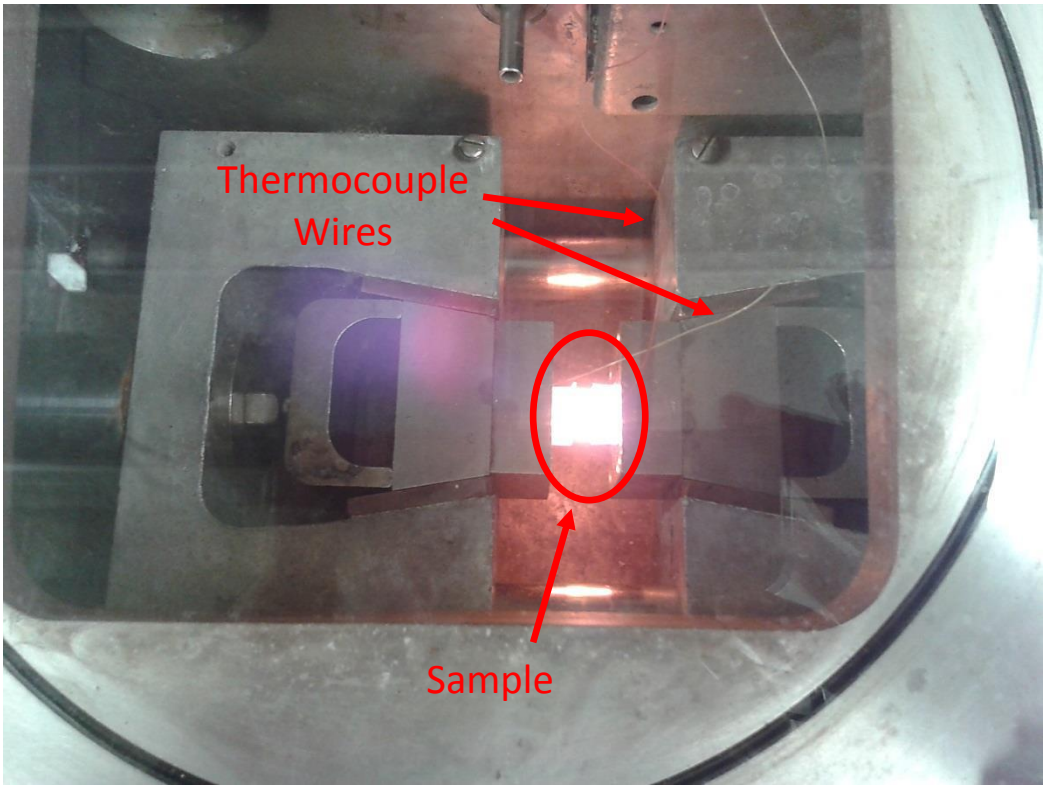

Figure 30: Gleeble 1500D used in this thesis

The surfaces of the sample in contact with the anvils are covered in tantalum foil to prevent diffusion of the anvil material into the sample. [16]. The sample size is approximately a third of a Transverse Rupture Strength (TRS) test bar (10.73mm X 13mm X 8mm). A typical sample can be seen in Figure 31 below.

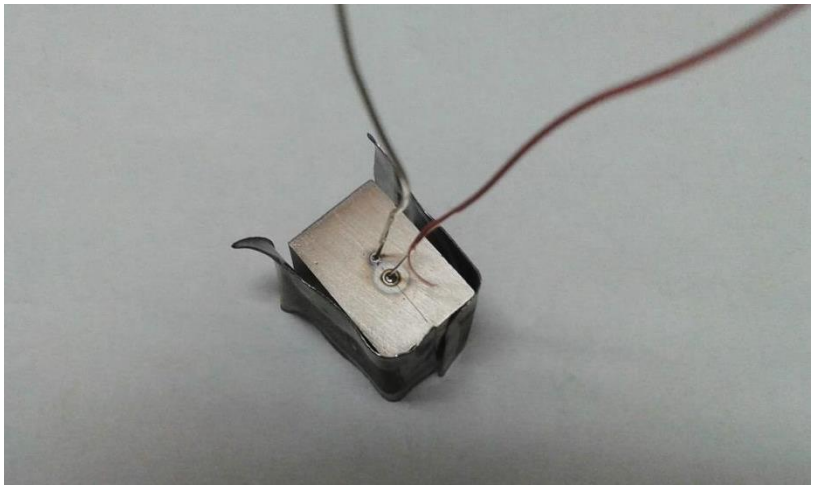

Figure 31: Thermocouple attachment used in this thesis

To minimize the effects of oxidation on the heated samples, the chamber was evacuated to approximately 4.5×10^{-4} Torr, flushed with argon and re-evacuated. At this point, a slight positive pressure of argon was introduced into the chamber to prevent the ingress of atmospheric oxygen.

This apparatus allows controlled deformation at temperature. In the present research, samples were deformed by 0% to 35% length at temperatures from 1200-1250˚C,

depending on the sample. The apparatus also allows quenching of the sample using an adjustable flow of either argon or water using the apparatus shown in Figure 32.

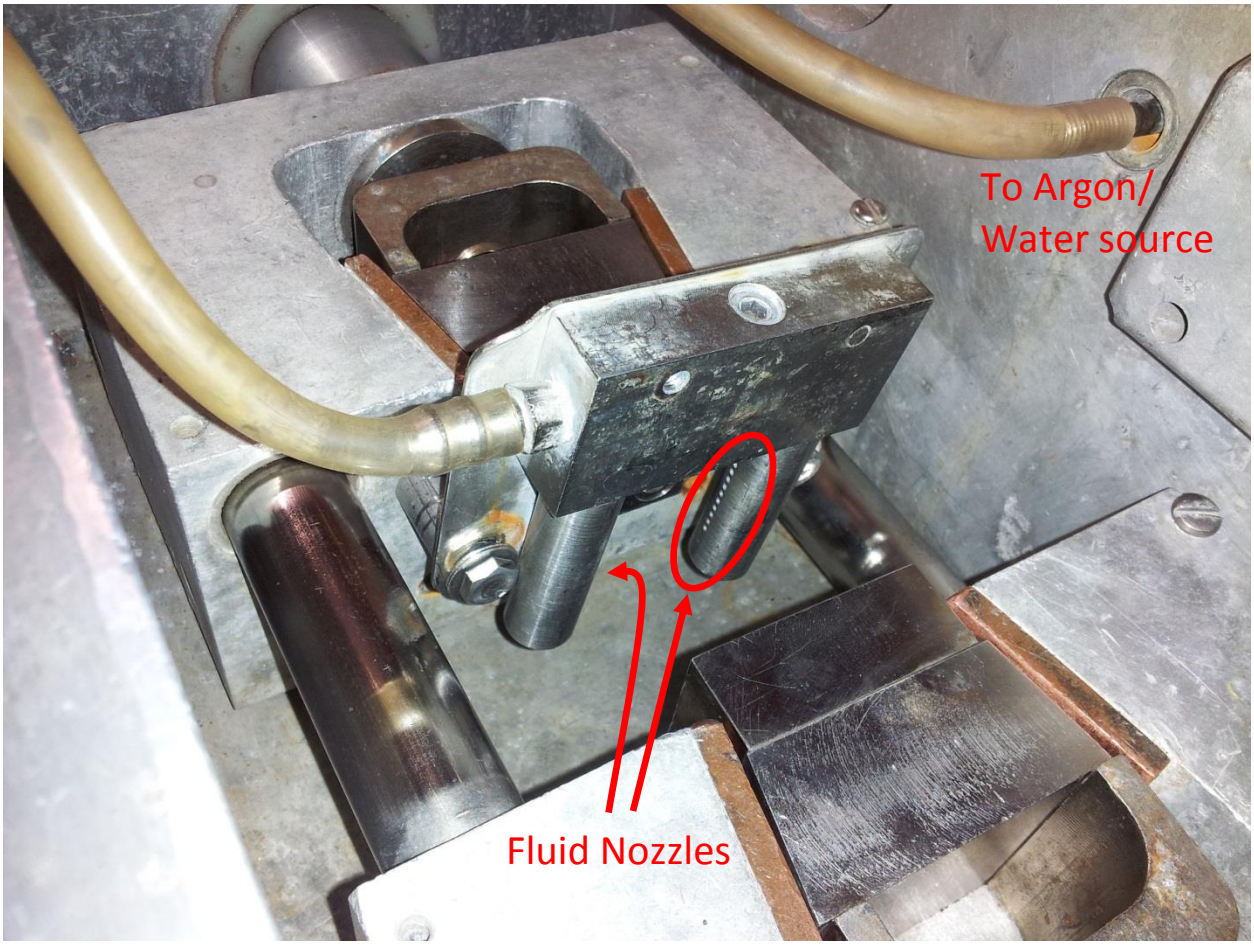

Figure 32: Gleeble 1500D quenching apparatus

4.6. Statistical Analysis and Furnace Heat Treatment

Hardness is an extremely important material property to control. As such, a heat treatment analysis was performed to better understand the relationship between the controlled variables, time (t) and temperature (T), and the resulting material hardness.

4.6.1. Statistical Design of Experiment

The zone of interest for heat treatment of this alloy was estimated to be from 800°C to 1000°C, and the optimal treatment length estimated to be within the range of 5-20h. As such, an experiment was designed (K. Mount, personal communication, 6 Dec 2012). The heat treatments were chosen to provide variations of a single variable at a time, to isolate the effect of a single parameter change on the resulting sample hardness. A block of eight heat treatments was performed in the center of the area of interest to take variability into account. A graphical representation of the data points used in this experiment is shown in Figure 33 below.

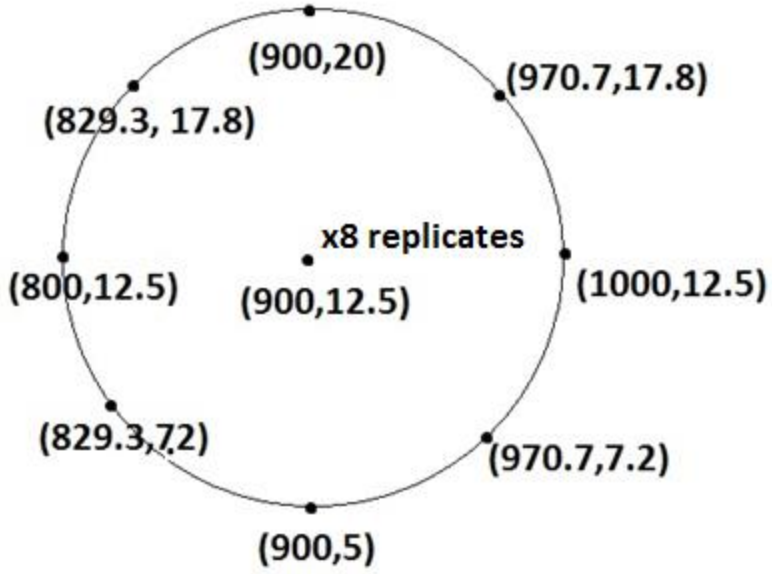

Figure 33: Heat treatment parameters, where [x,y] represents (T [°C], t[h])

To account for possible changes in environment over time, the heat treatments were performed in a randomized order. The parameters and order in which the heat treatments were performed can be found in Appendix A.

4.6.2. Furnace Heat Treatments

Following the design of the above experiment, samples were prepared for heat treatment. As-sintered samples were sections approx. 1.5mm thick sliced from source TRS-size as-sintered samples, machined using Electric Discharge Machining (EDM) to minimize deformation effects. Samples were enclosed in welded foil envelopes of stainless steel and then covered in high-temperature cement to minimize oxidation.

Hardness data were collected for each of the 16 samples, and a 3D surface plotted to show the relationship between temperature, time, and hardness (see Section 5.3). The complete data and hardness measurements (as per Section 4.9) can be found in Appendix A

4.7. Etching and Volumetric Point Count

Heat treatment samples were polished to 1µm diamond paste, or 0.05µm colloidal silica if the features to be examined were sufficiently small, and were etched in a solution of 12ml 70% H_3PO_4 + 40ml 70% HNO_3 + 48ml 98% H_2SO_4 at 5V for 1-5s depending on the size of the sample. This revealed microstructural features such as γ'.

Where appropriate, v/o of γ' precipitates and porosity values were obtained using a point count method with at least 100 points.

4.8. Density Measurements

To determine the density of a sample, the sample is first weighed in air (to approximate the mass of the sample). ESSO-NUTO H46 hydraulic oil was then used to infiltrate the sample, which is then re-weighed. The oil-impregnated sample was then weighed while

suspended in distilled water. The density was then calculated using the following equation:

$$\boldsymbol{\rho = \frac{M_{air} \times \rho_{water}}{M_{air/oil} - M_{water/oil}}} \quad \textbf{\textit{Equation 4}}$$

Where ρ is sample density, M_{air} is the weight of the sample in air, $M_{air/oil}$ is the weight of the oil-infiltrated sample in air and $M_{water/oil}$ is the weight of the oil-infiltrated sample in water, and ρ_{water} is the density of water:

$$\boldsymbol{\rho_{water} = 7 \times 10^{-8} T^3 - 1 \times 10^{-5} T^2 + 1 \times 10^{-4} T + 0.9996} \qquad \textbf{\textit{Equation 5}}$$

Where T is the temperature in °C. This method allows compensation for water infiltration into open porosity, and results in a more accurate density than simply weighing in water.

The percent theoretical density can then be calculated using a theoretical density of 8.22g/cm^3 obtained from the elemental ratios (see Section 4.1) and elemental densities (see Appendix C) using the "Rule of Mixtures" method.

4.9.Hardness Measurements

Hardness measurements were made to determine the presence or absence of γ'; these were obtained on a Vickers Micromet S104 micro-hardness tester (shown in Figure 34 below) with a 1kgf load.

Figure 34: Buehler Micromet S104 used in this thesis

The samples so tested were ground using 600 grit SiC paper, and then polished using 6µm diamond paste. A minimum of 10 readings were taken from each sample, with the

highest and lowest values dropped in accordance with standard practice for similar powder metallurgy products.

4.10. Scanning Electron Microscopy & Energy Dispersive Spectrometry

The scanning electron microscope used in this study was a JEOL 5900-LV, as shown in Figure 35 below. A working distance of approximately 11mm was used, with the electrons accelerated at 20kV of potential. Both Secondary Electron (SE) and Backscatter Electron (BSE) detectors were used for imaging. In addition, an Oxford Link Energy Dispersive Spectroscopy (EDS) detector running Oxford Instrument's INCA software was used to obtain elemental maps of the samples.

Figure 35: JEOL Scanning Electron Microscope used in this thesis

4.11. Atomic Force Microscopy (AFM)

Because the hardness data suggested the continued presence of γ' precipitates even following a solutionizing treatment, selected samples were examined using a Digital Instruments D3100 Atomic Force Microscope as shown in Figure 36 below.

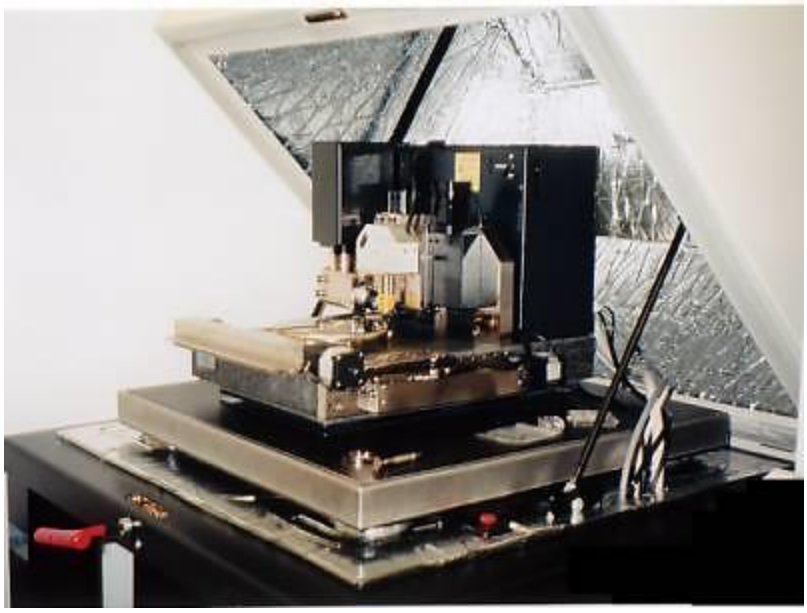

Figure 36: Digital Instruments D3100 AFM as used in this thesis [33]

Images were captured using the tapping mode to prevent damage to the probe tip from porosity or other sharp microstructural features in the samples. The cantilever used had a probe depth of 4µm and a tip radius of 10nm. The cantilever was driven at approximately 294 kHz, with an offset from the resonance frequency of 2%. The resulting images were captured after more than four minutes of continuous operation, to ensure that the piezoelectric controllers were at a steady-state temperature. Digital Instrument's Nanoscope software was used both for control of the AFM and post-experiment viewing and analysis.

4.12. ImageJ Image Analysis Software

ImageJ (version 1.51j8) is an open-source image processing and analysis software (available at imagej.nih.gov) that allows each precipitate in an image to be measured and characterised, and can output both summary data, and the characteristics of each precipitate.

This software was used to analyse the images taken using the Atomic Force Microscope to obtain detailed information on the Gamma Prime precipitates present in 6 samples having been subjected to different cooling rates.

After setting the correct scale and cropping the edges of the images, the Enhance Contrast tool was used. The images were then changed to 8-bit black and white images to allow the use of the Threshold tool, which turns the image into a binary particle-or-not-particle format. The Watershed tool was then used to separate precipitates. The Analyse Particles function was then used to output the area of each precipitate present in the images. Summary data are found in Appendix D, and the data are presented in Section 5.7.

5. Results and Discussion

This section presents the results of the original work performed in this thesis, and discusses the findings.

5.1. JMatPro Phase Modeling

Prior to the physical in-lab experiments, the behaviour of the TAS alloy (see Section 4.1 for alloy details) was modeled using JMatPro software (see Section 4.3 for details). The composition by weight of the TAS alloy was entered into the program. The phase composition of the alloy in was modeled with respect to temperature; the results can be seen in Figure 37 below.

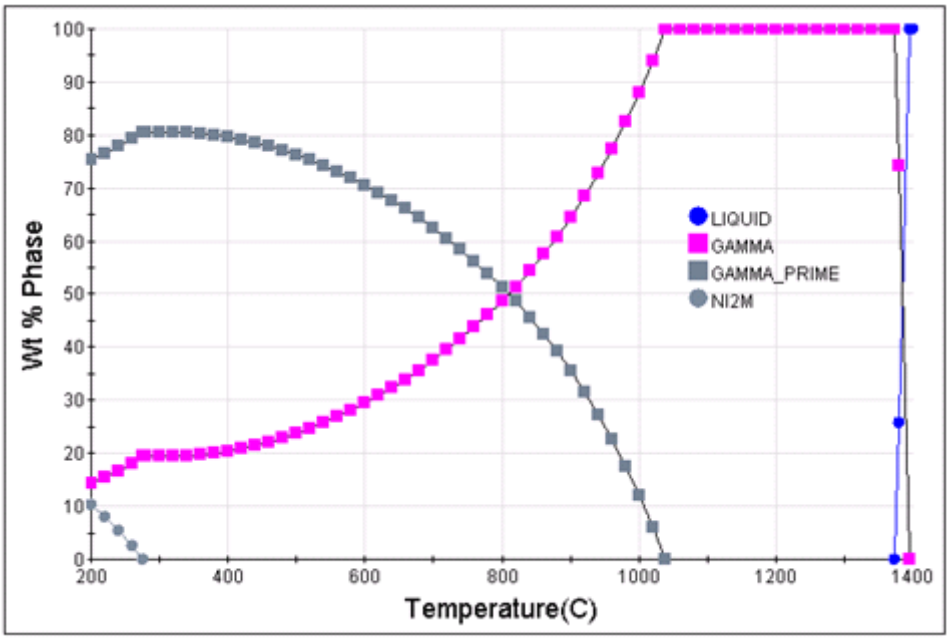

Figure 37: Phase composition of TAS alloy with respect to temperature

The JMatPro software assumes thermodynamic equilibrium for its calculations: it considers the alloy to be at a given temperature for an infinite amount of time for every evaluated temperature. In situations where the temperature may be changing rapidly, Figure 37 should be taken as an approximation and not as an absolutely predictive model. JMatPro predicts the solutionization temperature of Gamma Prime to be approximately 1040°C.

JMatPro's predicted phase composition (as shown in Figure 37) shows the Gamma Prime phase consisting of over 80% of the mass of the alloy at certain temperatures. This is greatly in excess of the measured values which were on the order of 30-55% depending on the heat treatment.

Another feature of the JMatPro software is its ability to calculate Continuous Cooling Transformation (CCT) curves. The curves for 50% and 60% Gamma Prime volume fractions are shown in Figure 38 and Figure 39 below.

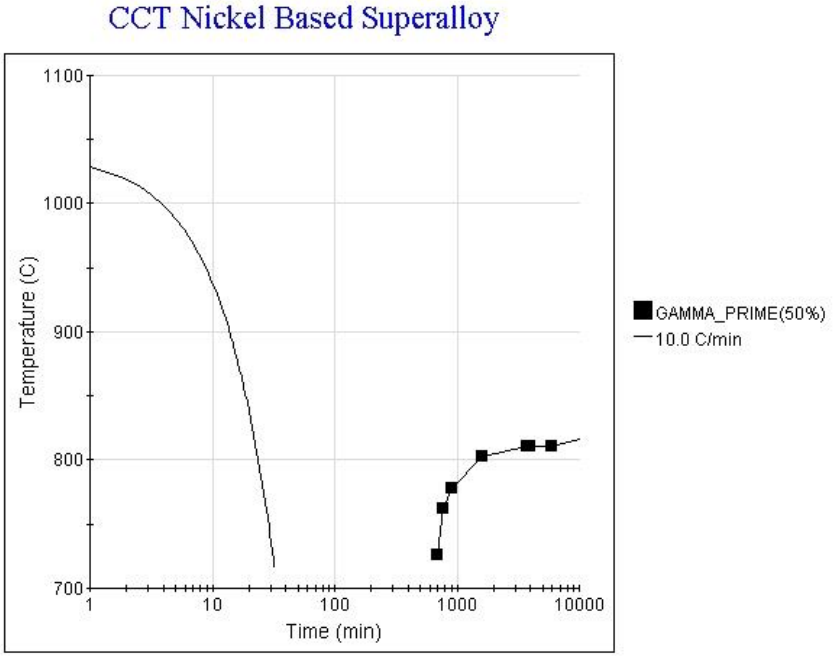

Figure 38: CCT curve for 50% Gamma Prime

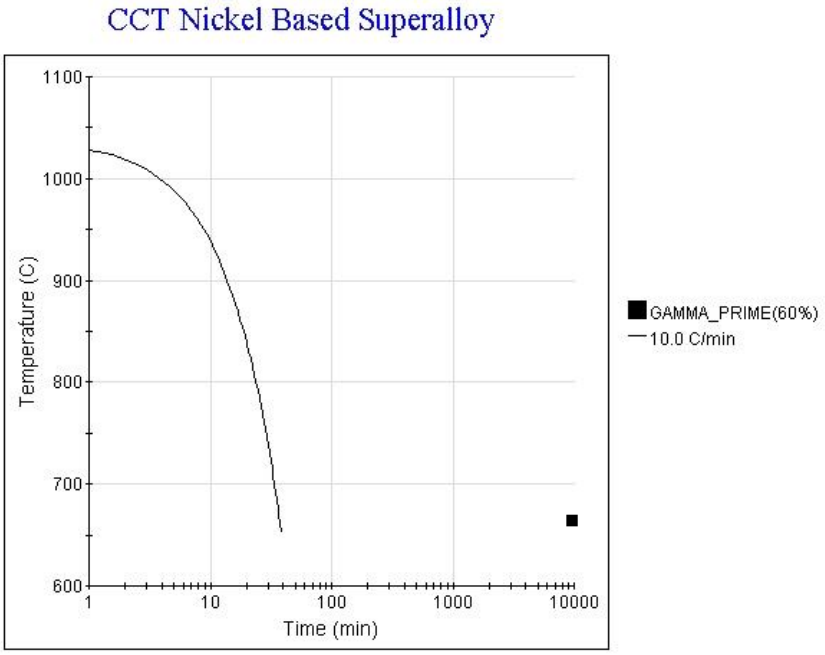

Figure 39: CCT curve for 60% Gamma Prime

As noted in Section 4.2.3 above, the alloy was cooled at 10°C/min after the sintering procedure. The weight fraction of Gamma Prime at room temperature as calculated by JMatPro (see Figure 37) is 75% in the TAS alloy. The CCT curves calculated by JMatPro however, show decidedly no intersection of the 10°/min line with the 60%, or even the 50% Gamma Prime fraction lines. These curves should therefore be viewed with the appropriate amount of scepticism.

5.2. Differential Scanning Calorimeter Analysis

To complement the information obtained from the JMatPro software, samples of TAS alloy were put through a DSC as per Section 4.4 above. The resulting data were processed to show the heat fluxes into and out of the sample when heating and cooling at a constant rate, as seen in Figure 40. Gradual changes in heat flux can indicate changes in heat capacity, while sharper spikes or dips can be indicative of phase changes.

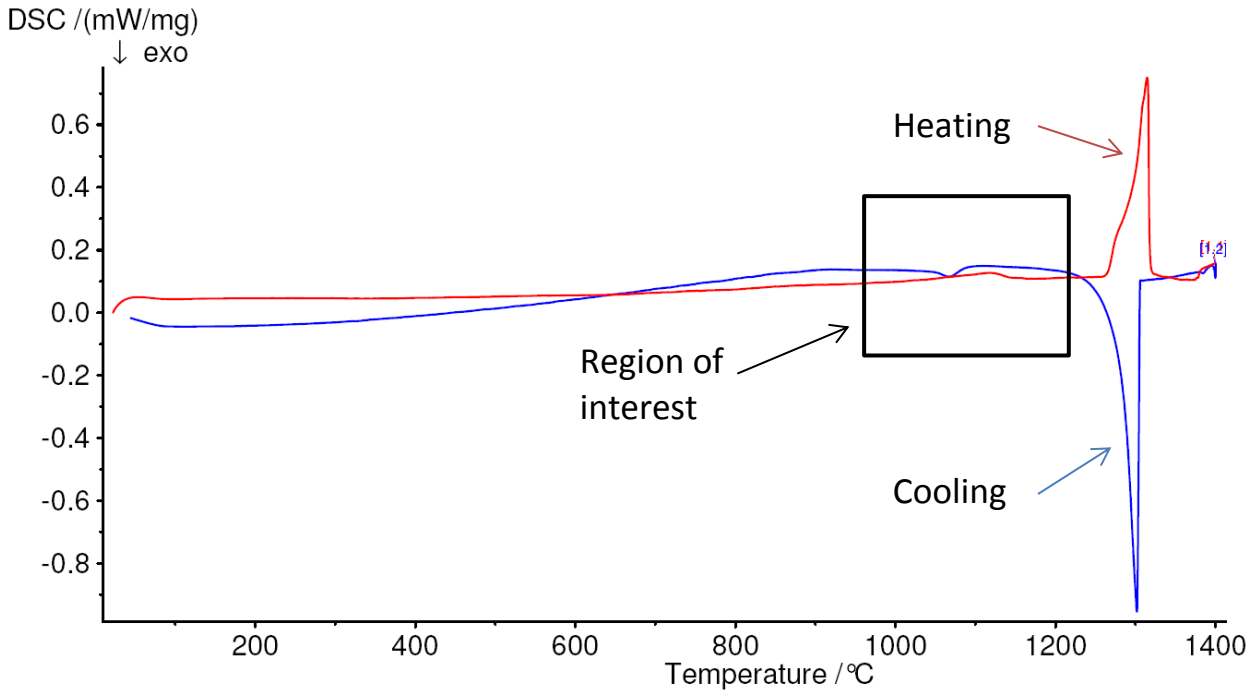

Figure 40: Full heat flux curve for TAS alloy

The large heat fluxes at 1300˚C indicate melting and solidification respectively. Of more interest are the much smaller heat flux discontinuities occurring near 1100˚C.

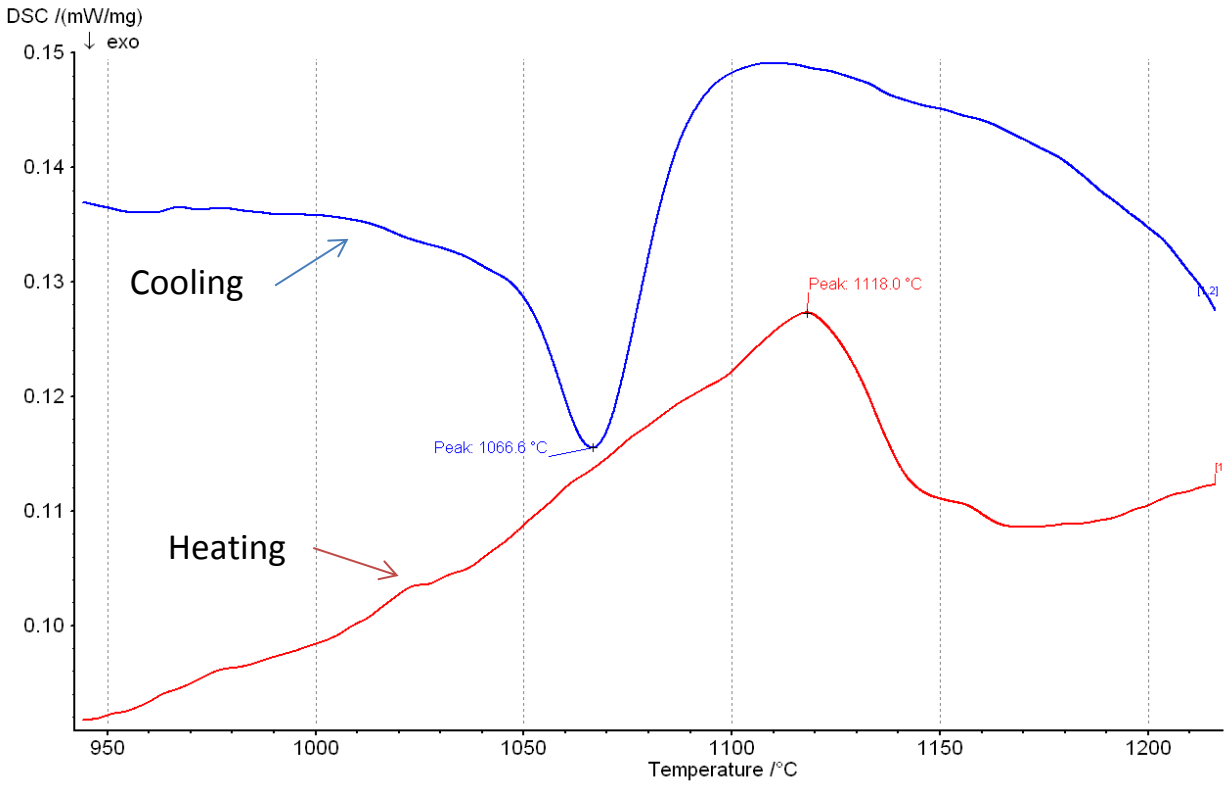

Figure 41: Heat flux curve around 1100° for TAS alloy

Using the approximate Gamma Prime solutionization temperature from JMatPro in Section 5.1, we can identify the discontinuities in the heat flux curve of Figure 41 as the points where the Gamma Prime phase solutionizes, and precipitates. Most of the difference between the heating and cooling peak flux temperatures is likely due to non-equilibrium effects. By averaging the heating and cooling peak, the DSC procedure gives an average phase change temperature of 1092˚C.

5.3. Statistical Analysis and Heat Treatment

Performing the heat-treatment outlined in Section 4.6 and subsequent hardness testing gave mean hardnesses and standard deviations for the 16 samples. Table 5 gives a summary of the data, with the complete set listed in Appendix A. The data were plotted using Matlab, and a 3D surface was created to help visualization using the Matlab Mesh function (Figure 42). The full data and code are available in Appendix B. It should be noted that the 8 points in the center of the region of interest were averaged to obtain better visibility in the graphed surface.

Table 5: Summary of post-HT hardnesses

Run #	Time (h)	Temp (°C)	Mean Hardness (HV)	Std Dev (HV)
1	12.5	900	366	31
2	12.5	900	332	19
3	12.5	900	314	26
4	5	900	319	28
5	20	900	346	40
6	12.5	1000	393	108
7	12.5	900	337	21
8	17.8	829	314	27
9	12.67	900	358	48
10	7.2	829	324	22
11	17.8	971	355	42
12	12.5	800	342	41
13	7.2	971	321	31
14	12.5	900	345	22
15	12.5	900	330	20
16	12.5	900	329	33

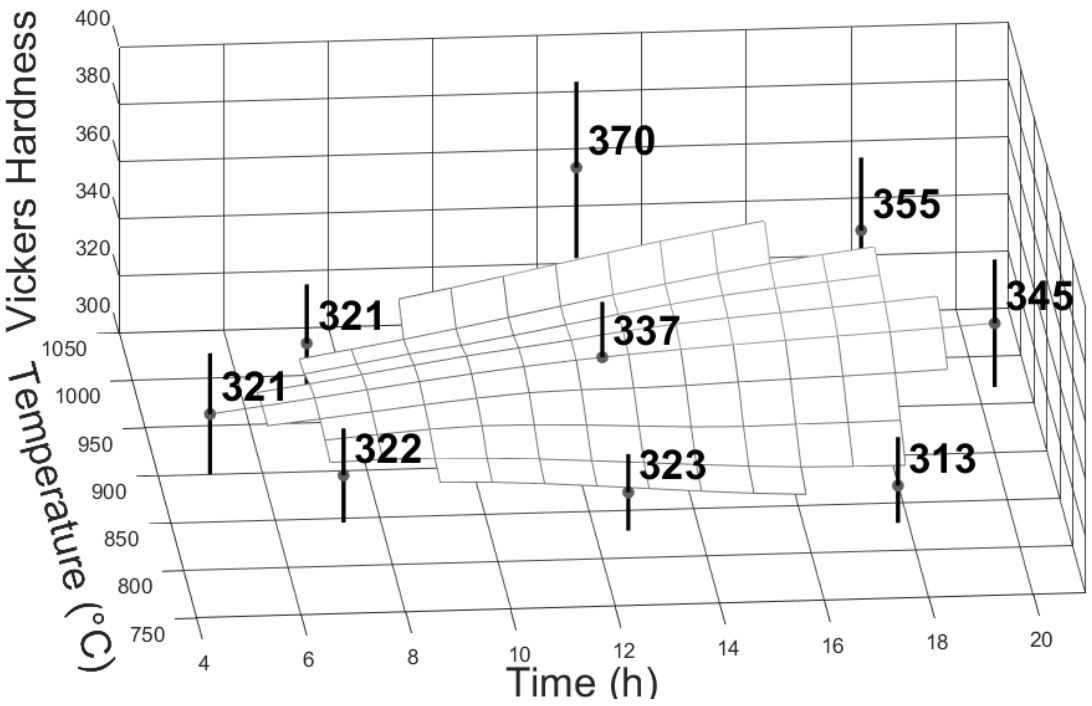

Figure 42: Plotted simplified post-HT hardness and 3D surface mesh

The vertical bars in Figure 42 indicate the standard deviation of the hardness measurements.

Looking at the surface mesh above, the sample hardness begins a sharp increase in the higher-temperature region of the area of interest. Conversely, the heat-treatment time shows a gradual, but steady increase in hardness. Comparing the hardnesses of orthogonal points (points where only one variable has changed) illustrates this effect.

It can therefore be concluded that, in heat treatment applications, proper temperature control is of superior importance to exact timing to obtain the desired microstructure size.

5.4. Consolidation: Uniaxial Press VS CIP

While uniaxial pressing of green PM parts is simple and can produce a greater throughput on production lines, cold isostatic pressing allows parts with less restricted geometry, as well as providing a more even compaction (see Figure 5).

Samples of TAS composition made from elemental powders (to avoid solid solution or precipitation strengthening during the compaction phase) were pressed at 400 MPA in both uniaxial and CIP apparatus.

Table 6: Green densities of Uniaxial VS CIP samples

Sample	Density (g/cm^3)	% of Theoretical Density
Uniaxial (400 Mpa) Elemental	6.07	73.9
CIP (400 Mpa) Elemental	6.50	79.1
Theoretical density of TAS	8.22	-

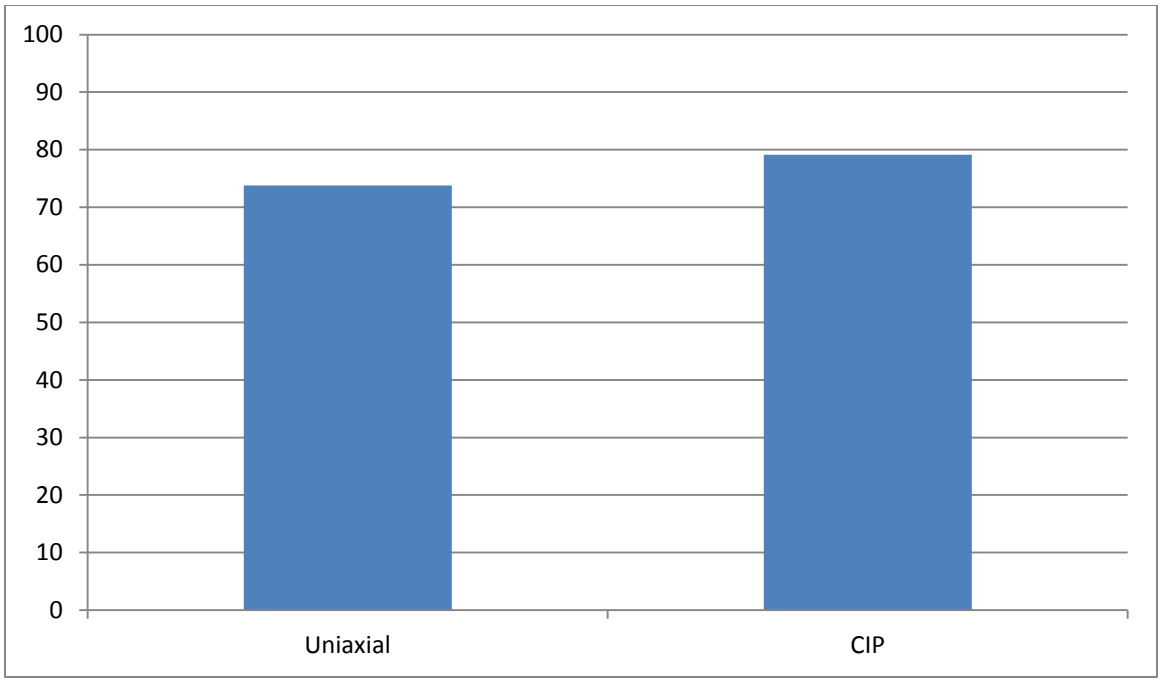

Figure 43: % Theoretical Densities of Uniaxial & CIP Green Samples

As expected, Table 6 and Figure 43 show that the CIP samples achieved higher density than a uniaxial-pressed sample at the same pressure, although both are still below 80% theoretical maximum density.

5.5. Master Alloy VS Elemental Powders

To determine the strengthening effect of pre-alloyed powders on green-sample compaction, samples were prepared using both pre-alloyed (masteralloy) and elemental powders (see Section 4.1). Compaction was performed at 500MPa in the uniaxial press, and 400MPa in the CIP apparatus.

Table 7: Green Densities of Masteralloy VS Elemental samples

Sample	Density (g/cm^3)	% of Theoretical Density
Uniaxial (500 MPa) Masteralloy	6.40	77.9
Uniaxial (500 MPa) Elemental	6.30	76.6
CIP (400 Mpa) Masteralloy	6.21	75.5
CIP (400 Mpa) Elemental	6.50	79.1
Theoretical density of TAS	8.22	

The elemental powder mix achieved 1.3% less theoretical density in the uniaxial apparatus, and achieved 3.6% more theoretical density in the CIP apparatus. There does not appear to be a significant advantage obtained by using elemental powders over pre-alloyed powders.

5.6. Atomic Force Microscopy

After samples were heated and rapidly cooled in the Gleeble apparatus, Gamma Prime precipitates could not be resolved using an SEM microscope (Figure 44), or an Auger microscope (Figure 45).

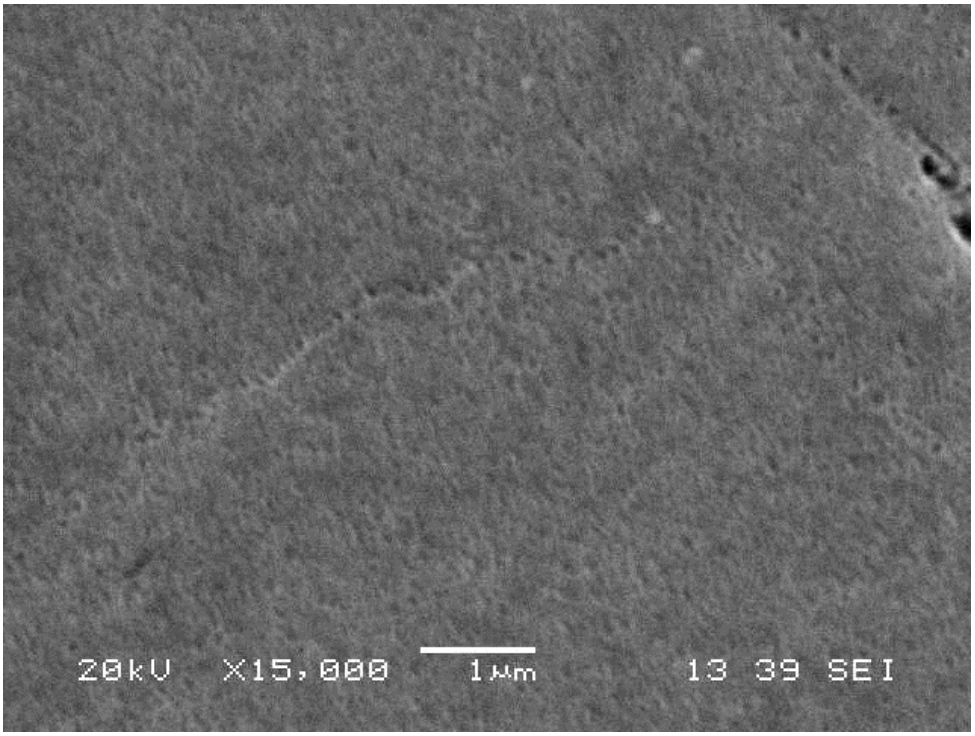

Figure 44: SEM micrograph of a water-quenched TAS sample at 15000x magnification

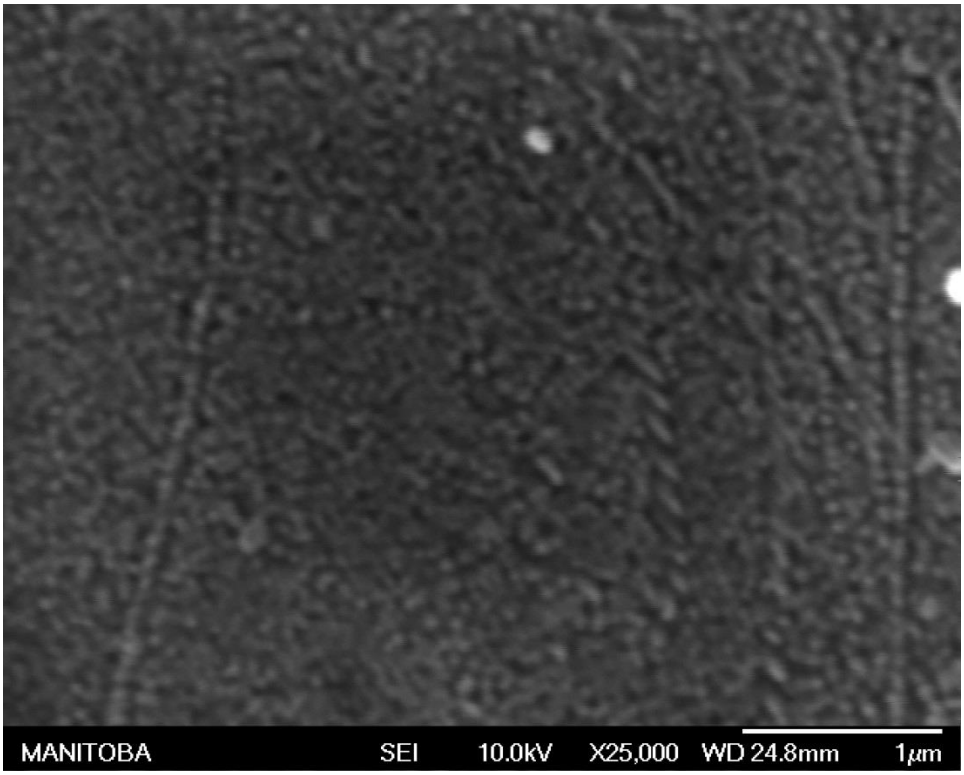

Figure 45: Auger micrograph of an air-cooled TAS sample at 25000x magnification

Using an AFM in tapping mode as described in Section 4.11, Gamma Prime precipitates in the 10-90nm scale could be resolved, as shown in Figure 46 through Figure 48. Precipitate size and distribution analysis are given in Section 5.7.

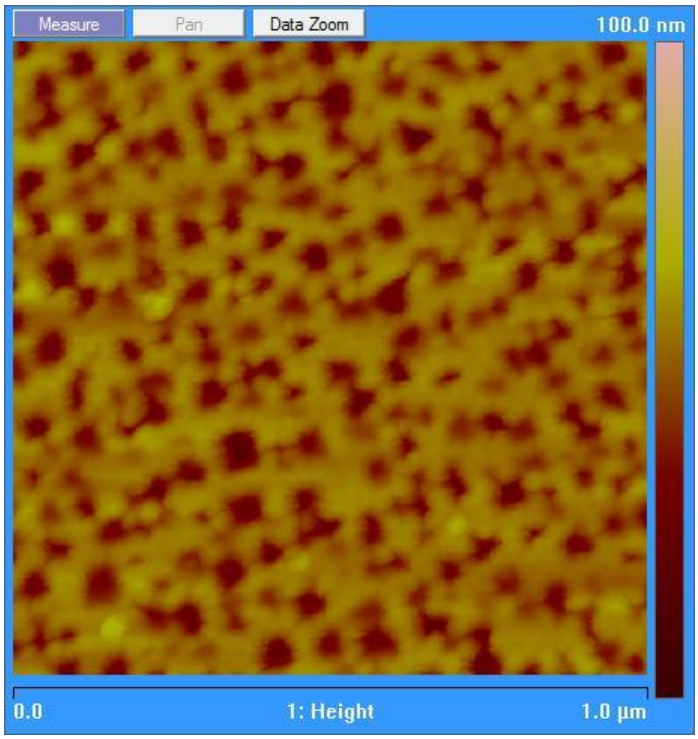

Figure 46: AFM micrograph of water-cooled TAS sample (Sample #1)

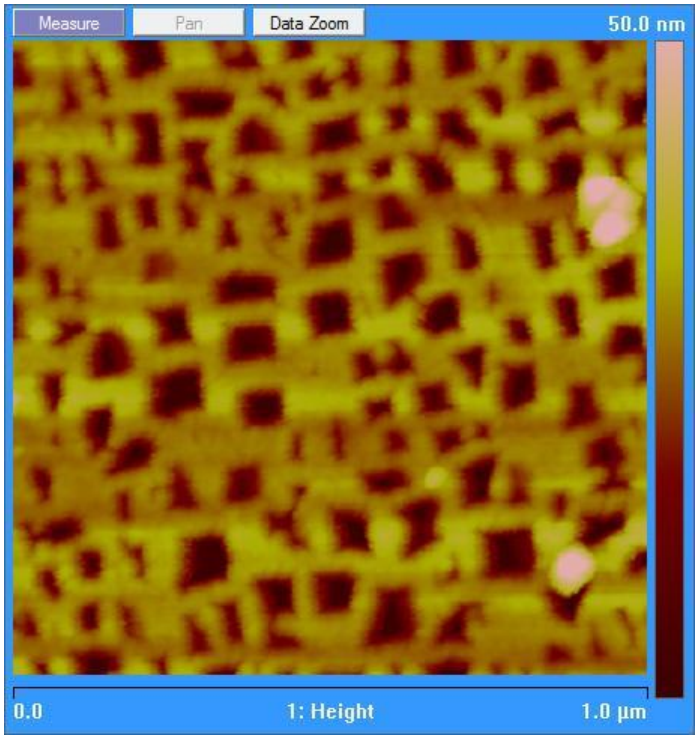

Figure 47: AFM micrograph of high-flow argon-cooled TAS sample (Sample #2)

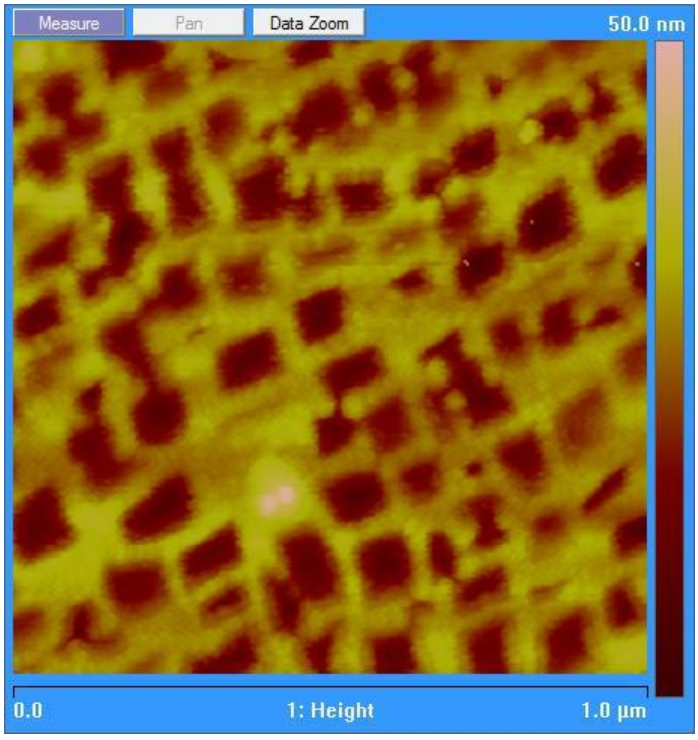

Figure 48: AFM micrograph of low-flow argon-cooled TAS sample (Sample #5)

Using an AFM to image the small Gamma Prime population allows the use of the same sample preparation methods as for high-magnification SEM imaging: polishing through to 0.05µm colloidal silica followed by an electrolytic etch (see Section 4.7). This bypasses the need for microtome or ion milling operations as would be required for a TEM. This allows more efficient use of samples, and quicker sample preparation times.

The raw data included in an AFM micrograph includes cantilever height data. As such it is possible to create a topographical map instead of simply looking at a 2D representation. Figure 49 below shows a 1µm x 1µm topographical map of a γ' precipitate as found in an as-sintered sample. It is easy to see that the electrolytic etch preferentially attacks the γ' precipitate over the γ matrix, and the increased etch depth at high-energy boundary regions, all as expected.

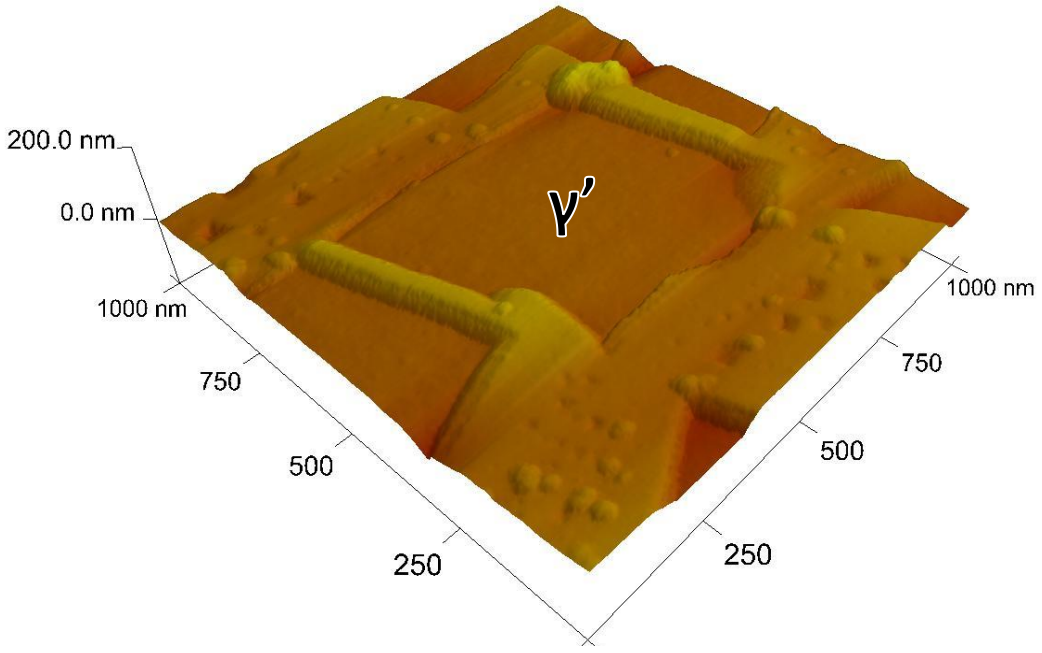

Figure 49: AFM topography of a preferentially attacked γ' precipitate in as-sintered sample

5.7. Precipitate Size Distribution

The raw data used in this analysis were obtained using ImageJ image analysis software (see Section 4.12), and are available in Appendix D. Table 8 lists the average precipitate diameters and volume fractions for each sample analyzed. The precipitates cross-sections were assumed to be circular, and precipitates with sub-10nm diameters were removed before averaging to eliminate low-pixel-count artifacts; the size distributions in Figure 52 through Figure 57 give justification for this omission. Figure 58 gives the average precipitate diameter, while Figure 59 lists the Gamma Prime volume fraction, both in relation to the cooling rate (please note that the cooling-rate axis is logarithmic).

Table 8: Average Cooling Rates, Average Precipitate Sizes and γ' Volume Fractions for AFM Samples

Sample #	**1**	**2**	**3**	**4**	**5**	**6**
Avg Cool Rate (°C/s)	176	123	13.4	15.1	7.5	8.3
Precipitate Diameter (nm)	40.9	49.0	51.6	53.5	58.3	62.8
Gamma Prime Volume Fraction (%)	27.3	25.1	25.7	25.4	27.7	28.8

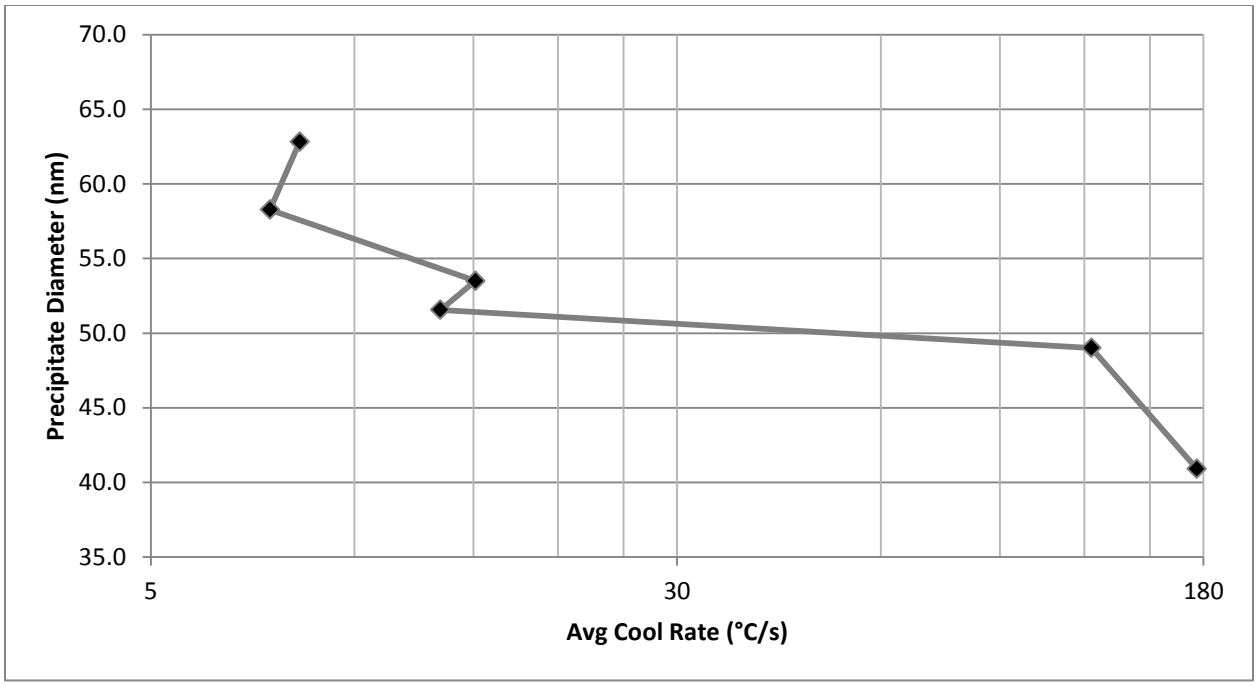

Figure 50: Average Precipitate Diameter (nm) vs Avg Cool Rate (°C/s)

As expected, Figure 50 shows that increasing the cooling rate results in a definite trend towards decreasing particle size.

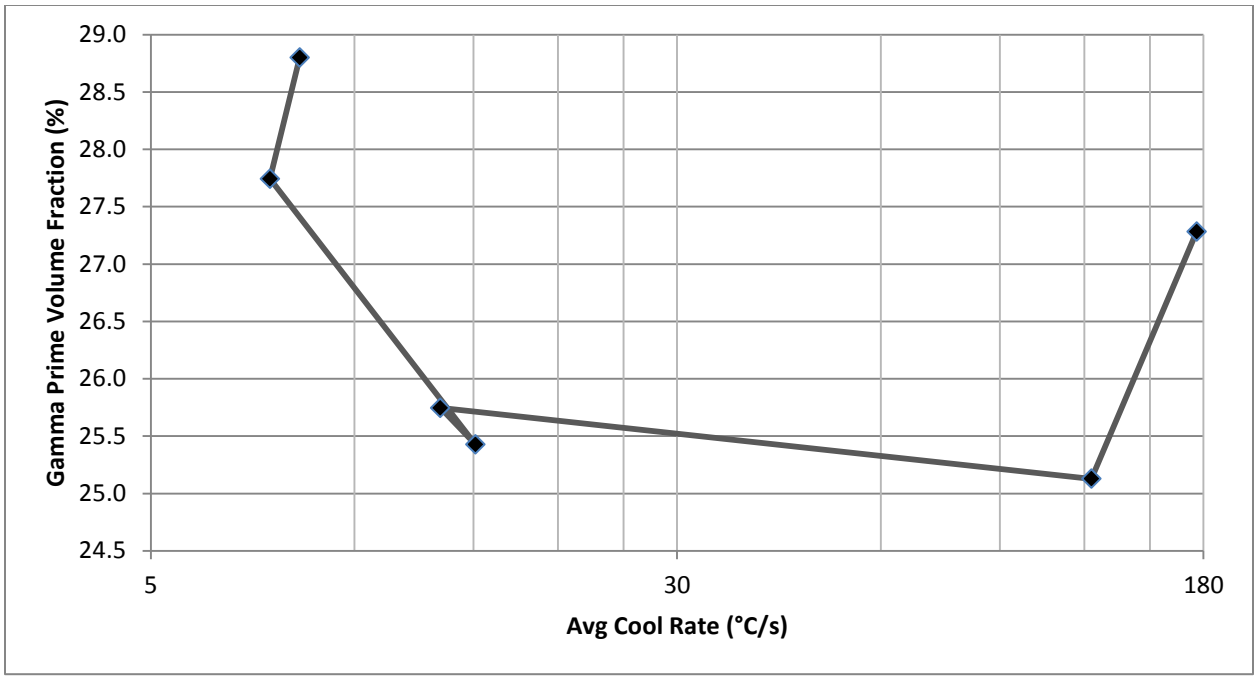

Figure 51: Gamma Prime Volume Fraction (%) vs Avg Cool Rate (°C/s)

Figure 51 shows that in the range of cooling rates observed in this thesis, the volume fraction of Gamma Prime does not show a close relationship to cooling rates, unlike the slower rates used commercially [27].

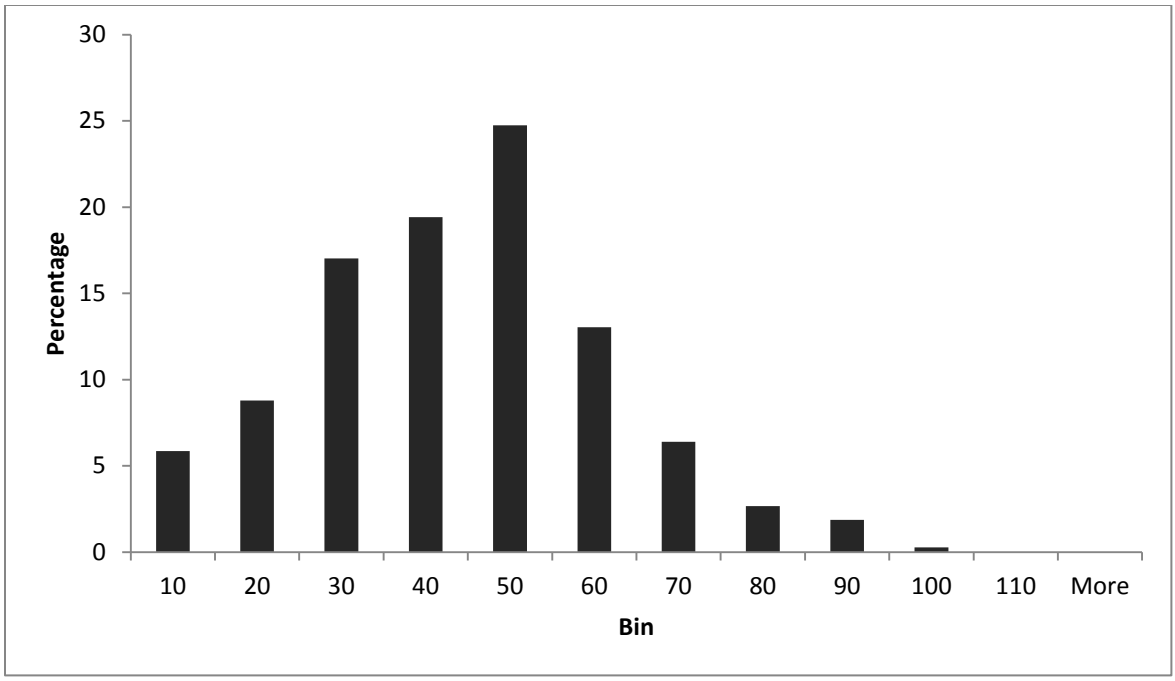

Figure 52: Precipitate Size Distribution for Sample 1 (176 °C/s) where a Bin represents a 10nm range

As Figure 52 shows the size distribution for the fastest-cooling sample, a bias towards the smaller precipitate sizes is expected. The precipitate frequency peaks in the 40-50nm range and decreases rapidly thereafter.

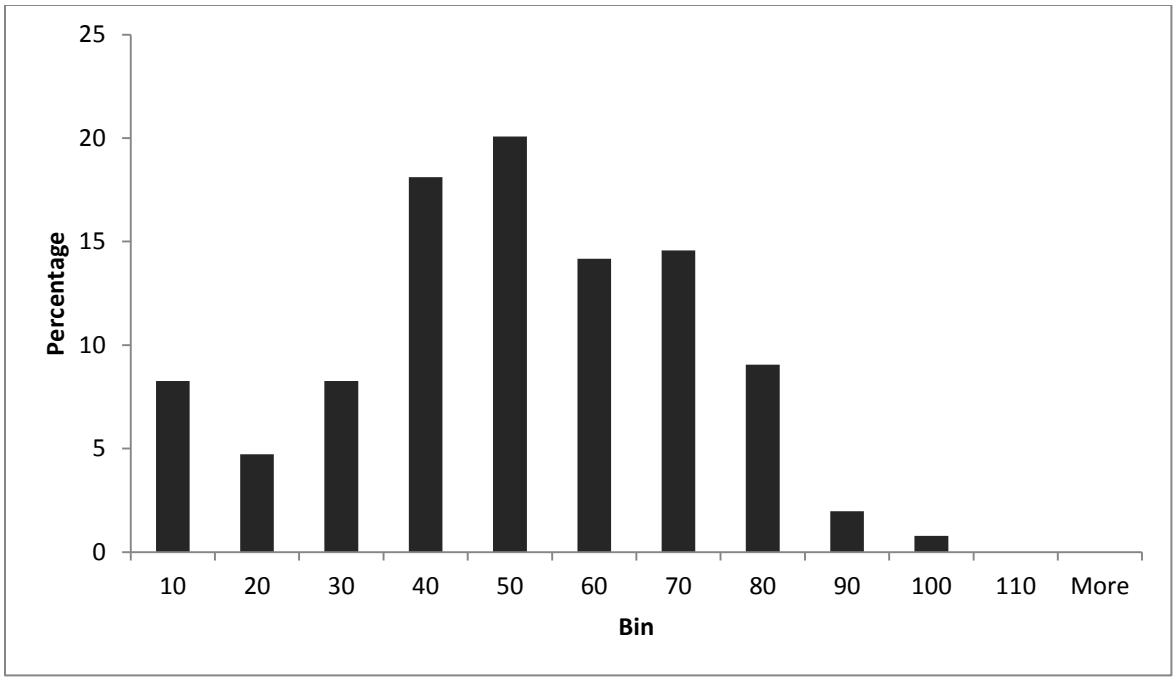

Figure 53: Precipitate Size Distribution for Sample 2 (123 °C/s) where a Bin represents a 10nm range

As the cooling rate decreases for Figure 53, a spike in particles smaller than 10nm can be observed. The precipitate frequency is still peaking in the 40-50nm range, but the decrease in larger particles is significantly more gradual compared to Sample 1 shown in Figure 52.

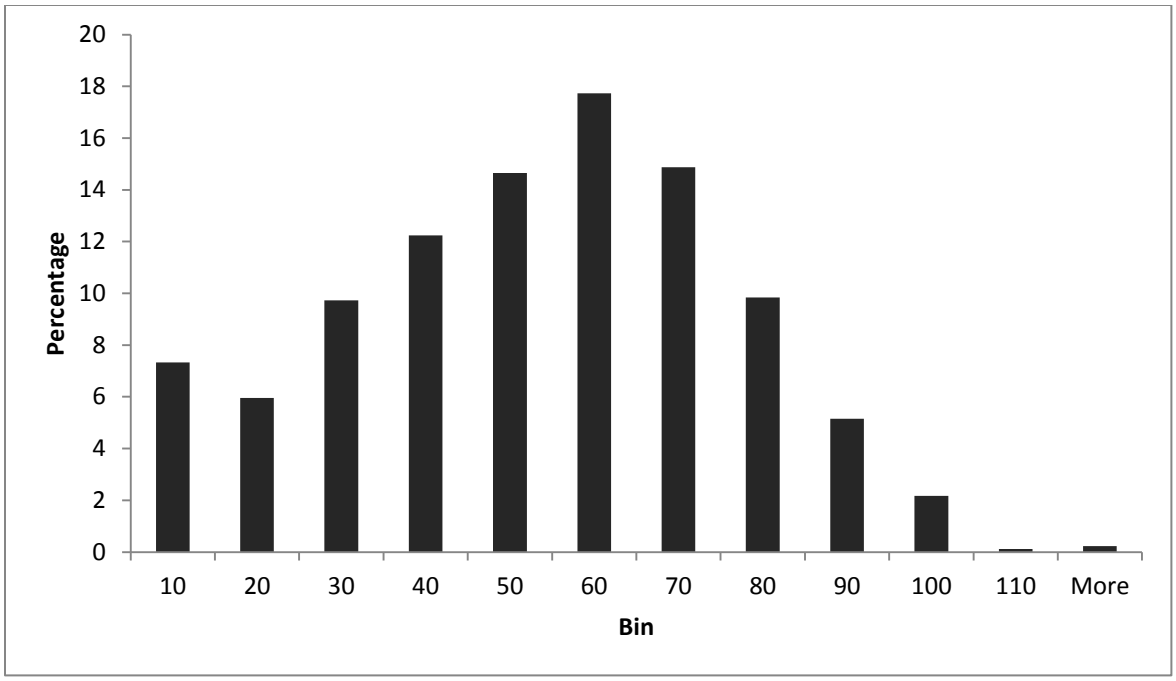

Figure 54: Precipitate Size Distribution for Sample 3 (13.4 °C/s) where a Bin represents a 10nm range

With a lower cooling rate, Figure 54 shows a nearly symmetric size distribution (save for the <10nm particles), with the peak observed in the 50-60nm range.

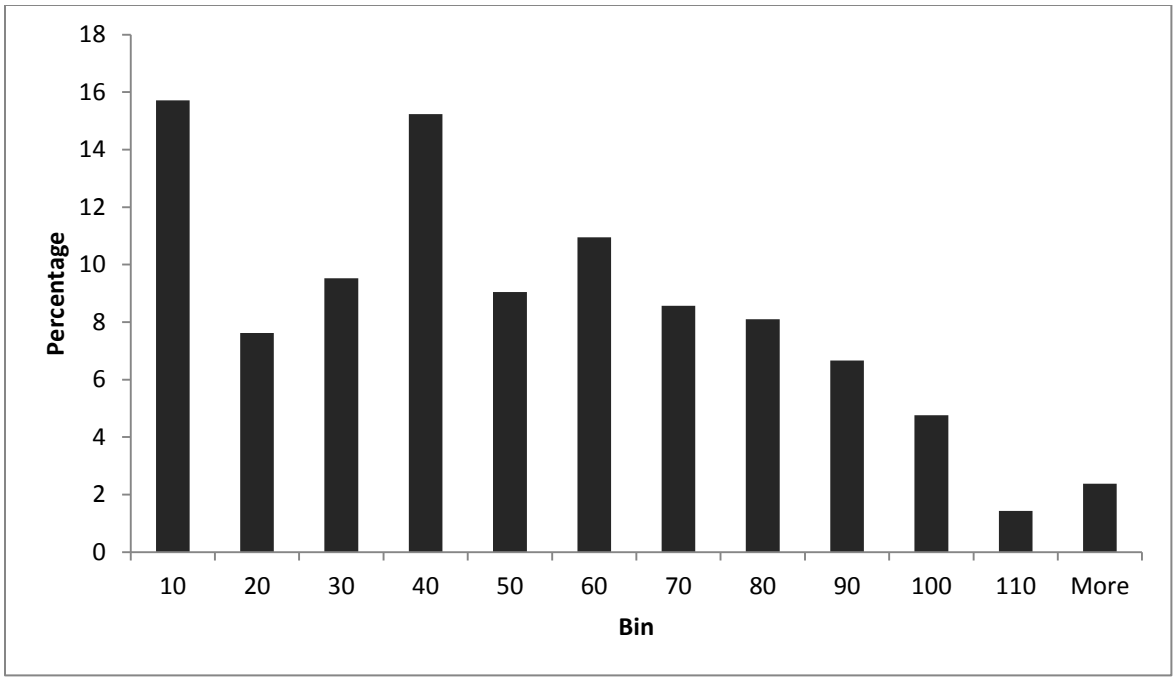

Figure 55: Precipitate Size Distribution for Sample 4 (15.1 °C/s) where a Bin represents a 10nm range

A similar distribution can be seen for Figure 55, with an anomalous spike in the 30-40nm range. The peak remains in the 50-60nm range.

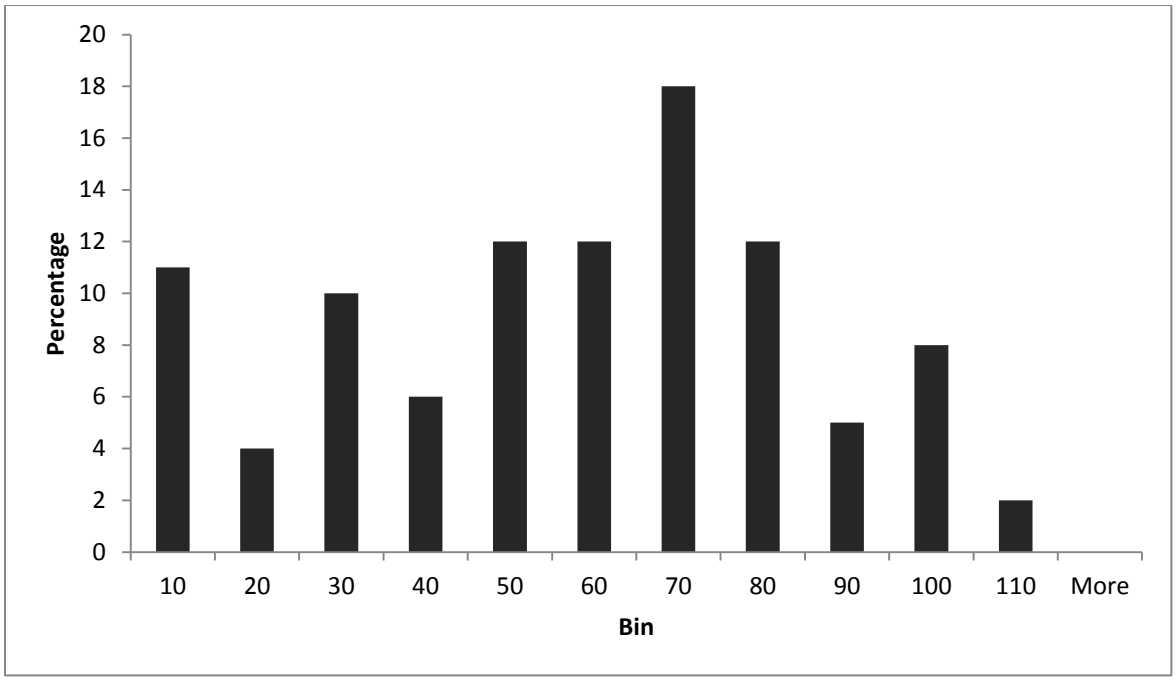

Figure 56: Precipitate Size Distribution for Sample 5 (7.5 °C/s) where a Bin represents a 10nm range

As the cooling rate decreases for Figure 56, the precipitate distribution widens as the precipitate size increases- the peak is now in the 60-70nm range.

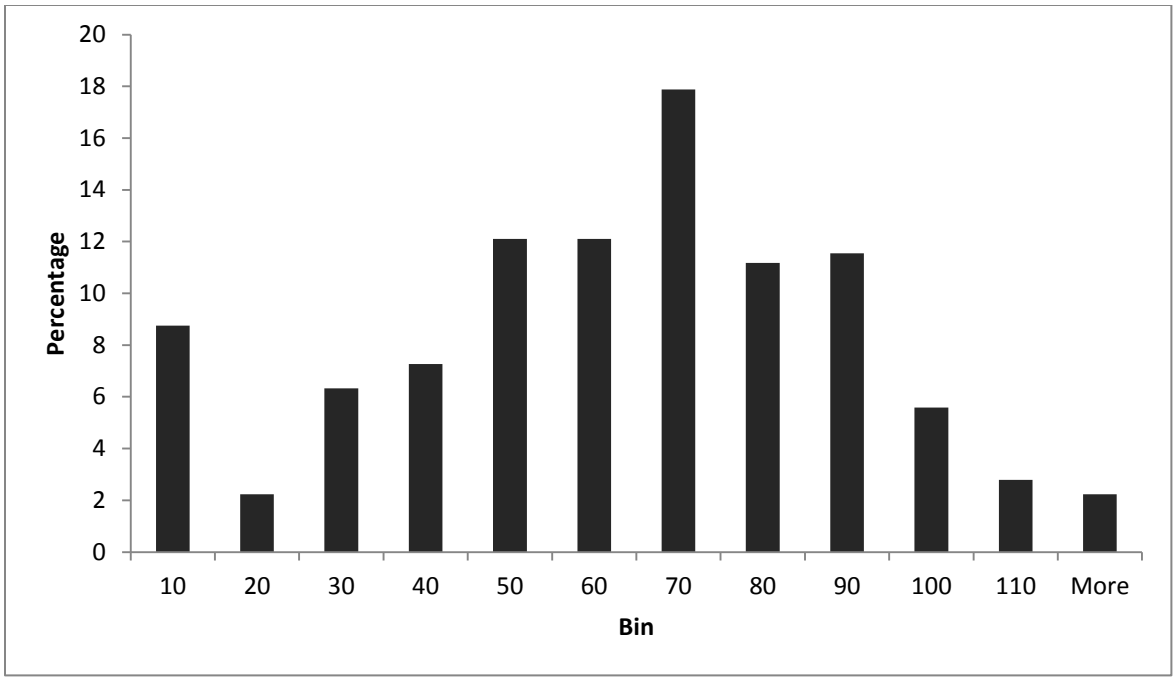

Figure 57: Precipitate Size Distribution for Sample 6 (8.3 °C/s) where a Bin represents a 10nm range

Figure 57 shows a similarly broad distribution, with the peak remaining in the 60-70nm range.

5.8. Gleeble Thermomechanical Testing and Density determination

To evaluate the effect of thermomechanical processing on sample density, samples of TAS were heated and compressed using the Gleeble 1500D apparatus (see Section 4.5).

Samples were heated to 1200°C, and compressed by 30% over 2s (rapid compression, see Table 9) and 60s (slow compression, see Table 10) respectively. Samples deformed by more than 30% were subject to rupture (see Figure 58).

Table 9: Pre- and Post-processing densities of TAS sample with rapid (2s) compression

	Average Density (g/cm^3):	Std Dev (g/cm^3):	% Theoretical density:
As Sintered	7.17	0.00737	87.3
2s Compression	7.40	0.0201	90.0

Table 10: Pre- and Post-processing densities of TAS sample with slow (60s) compression

	Average Density (g/cm^3):	Std Dev (g/cm^3):	% Theoretical density:
As Sintered	7.08	0.0818	86.1
60s Compression	7.45	0.0864	90. 7

The density increase using the rapid compression process was approximately 3.6%, compared with approximately 5.3% using the slow compression method. Increasing density using this method results in appreciable improvements, but significant porosity still remains.

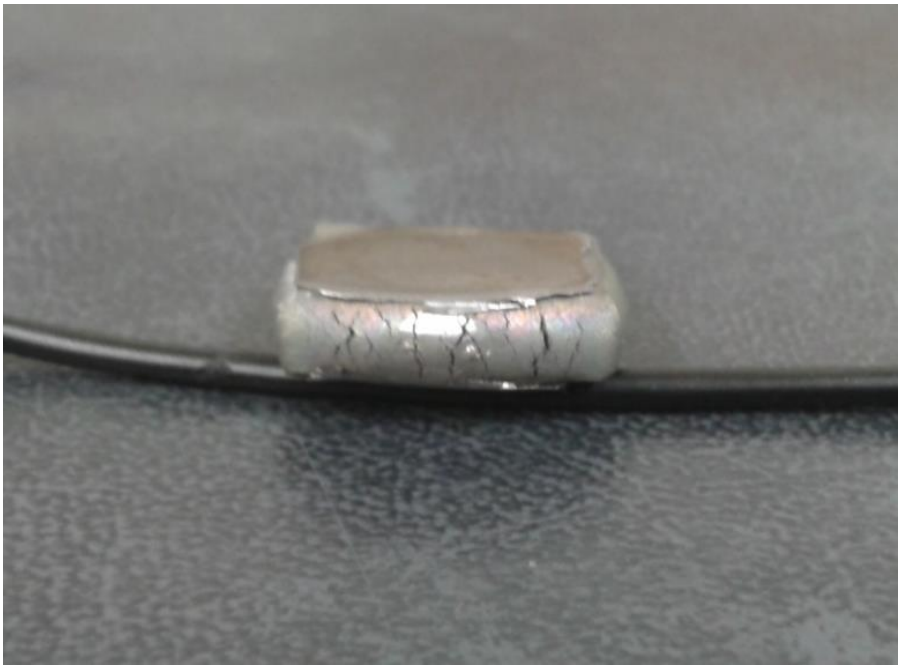

Figure 58: Representative Ruptured Sample Occurring at >30% Deformation at 1200°C

The apparent limit of 30% deformation restricts the use of post-sintering thermo-mechanical processing of PM products.

5.9. General Observations

Cr-Rich Phase

An unidentified third phase was also present in all TAS samples. This phase appears as the lighter-coloured areas in Figure 59 below.

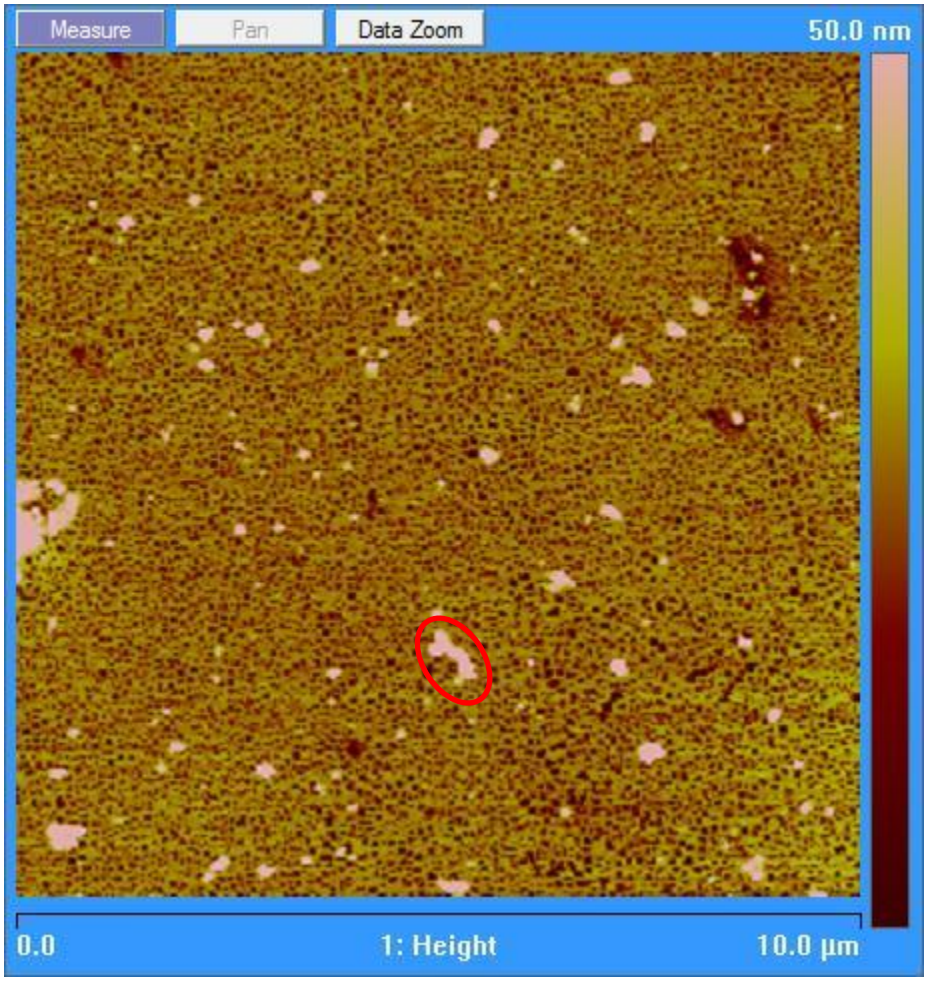

Figure 59: 10um AFM Micrograph of Water-Quenched TAS Sample showing representative Unknown Third Phase

An EDS elemental map (see Section 4.10) was performed to evaluate the composition of this third phase.

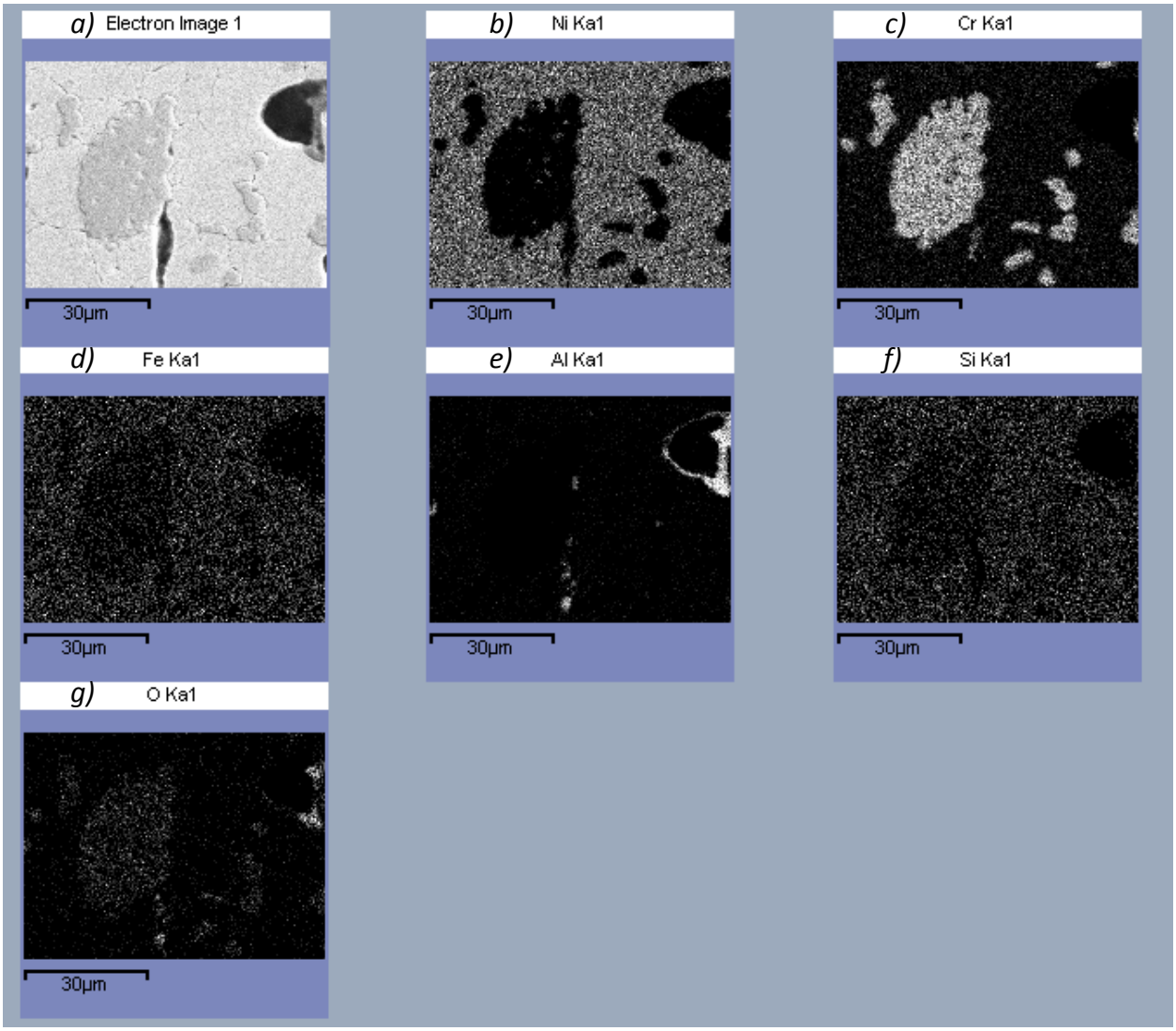

Figure 60: EDS Elemental Map of a Cr-Rich Phase

According to the EDS elemental map shown in Figure 60, this third phase is strongly chromium-rich (shown in image *c)*), and also shows increased oxygen content (shown in image *g)*). The

observations are consistent with this phase being Cr_2O_3. As this compound melts at 2435°C [8], it is no surprise that this phase remains out of solution even in samples that have been brought to 1200°C for a minute in the Gleeble apparatus or 1000°C for 12.5h in a furnace.

This phase was also noted by D.C. Murray in the un-sintered powders similar to those used in this thesis [16].

6. Conclusions

The following conclusions can be drawn from this work:

1. The modeling software JMatPro was very useful in determining the temperature range at which the Gamma Prime precipitates undergo solutionization. However, the predicted amount of Gamma Prime is much greater than that observed, likely because JMatPro assumes thermodynamic equilibrium for a process which is in reality kinetics-based.
2. A Differential Scanning Calorimeter was able to increase the precision of the solutionization temperature of Gamma Prime (observed to be 1092˚C)
3. Through statistical analysis of samples hardnesses following various heat treatments, it was found that the aging temperature has a much larger effect than ageing time, and so temperature management is the overriding concern during heat treatments.
4. As expected, cold isostatic pressing achieves higher green-body densities than uniaxial pressing. However, neither elemental or masteralloy powders appear to have a significant advantage in green density.
5. The use of an Atomic Force Microscope allowed the resolution of precipitates at sub-30nm scales, which greatly improved the ability to characterize Gamma Prime in samples that underwent more rapid cooling following precipitate solutionization. Additionally, AFM sample preparation is much simpler (and faster) in contrast to the TEM sample preparation allowing similar resolution.
6. As expected, the precipitate sizes were found to increase in size, and the distribution to widen with decreasing cooling rates.

7. Thermomechanical deformation was found to reliably increase sintered sample density (3.6% - 5.3% increases). However, deformation could not exceed 30%, limiting the uses of this technique.
8. Powder metallurgy, as a process, allows an excellent near-net-shape approach to replicate desirable microstructure found in Ni-based superalloys. However, in spite of investigating various techniques such as using unalloyed powders for sintering, varying green-body compaction parameters, and using the Gleeble apparatus as a hot-forging method to reduce porosity, significant residual porosity remained in the samples.

7. Future Work

Further work should be pursued in the following areas:

- During thermomechanical deformation, the thermocouple should be arranged as to measure the internal temperature of the sample, rather than the surface temperature to provide more accurate data. This might be performed by inserting a thermocouple coated with thermally conductive but electrically resistive material into the center of the sample. This could allow the creation of a useful practical formula to predict precipitate size in situations with non-steady rapid cooling rates.
- Further densification work should focus on increasing green-body density. Thermomechanical post-sinter processing achieved a density increase of 5.3%, comparable with the increase of 5.2% observed when using CIP instead of uniaxial pressing. As density changes during the sintering process result in associated dimensional changes, this is further incentive to maximize densification at the green-body stage.
- Further DSC experiments should be performed, with a slower rate of temperature change to increase the accuracy of the Gamma Prime solutionization temperature.

References

[1] Johnson Matthey Public Limited Company, "The PGM Database," [Online]. Available: http://www.pgmdatabase.com/jmpgm/index.jsp. [Accessed 6 December 2013].

[2] R. M. German, Powder Metallurgy Science, Princeton: Metal Powder Industries Federation, 1984.

[3] C. T. Sims, N. Stoloff and W. Hagel, Superalloys II: High-Temperature Materials for Aerospace and Industrial Power, John Wiley & Sons, Inc., 1987.

[4] Alfa Aesar, "Powder Products," [Online]. Available: http://www.alfa.com/en/gp140w.pgm?task=limitcat&catfilt=PURE. [Accessed 6 March 2014].

[5] D. C. Murray, N. L. Richards and W. F. Caley, "On the oxidation resistance of a powder metallurgy nickel-based superalloy," *Canadian Metallurgical Quarterly,* vol. 4, no. 52, pp. 439-448, 2013.

[6] R. M. German, Sintering Theory and Practice, New York: John Wiley and Sons Inc., 1996.

[7] Y. Nakagawa, "Aero-engine business and material technologies in Japan," in *Proceedings of the International Symposium on Superalloys*, 2004.

[8] The Materials Society, "Superalloys: A Primer and History," [Online]. Available: http://www.tms.org/meetings/specialty/superalloys2000/superalloyshistory.html.

[Accessed 02 March 2014].

[9] Combined Cycle Journal, "Consider replication to verify metallurgy of bucket blades after restoration heat treatment," [Online]. Available: http://www.ccj-online.com/consider-replication-to-verify-metallurgy-of-bucketsblades-after-restoration-heat-treatment. [Accessed 1 March 2014].

[10] P. Nash, M. F. Singleton and J. L. Murray, "Al-Ni Binary Phase Diagram," in *ASM Handbook Volume 3*, ASM International, 1991, pp. 112-115.

[11] R. Darolia, D. F. Lahrman and R. D. Field, "Formation of topologically closed packed phases in nickel base single crystal superalloys," *Superalloys,* pp. 255-264, 1988.

[12] Q. Shi, X. Ding, J. Chen, X. Zhang, Y. Zheng and Q. Feng, "Fracture Mode of a Ni-Based Single Crystal Superalloy Containing Topologically Close-Packed Phases at Ambient Temperature," *Metallurgical and Materials Transactions A,* vol. 45, no. 4, pp. 1665-1669, 2014.

[13] W. . D. J. Callister, Materials Science and Engineering: an Introduction, 7th ed., John Wiley and Sons Inc., 2007.

[14] Brush Wellman Inc., "Solid Solution Hardening & Strength," April 2010. [Online]. Available: http://materion.com/~/media/Files/PDFs/Alloy/Newsletters/Technical%20Tidbits/Issue%20No%2016%20Solid%20Solution%20Hardening%20%20Strength. [Accessed 24 December 2013].

[15] A. M. Donald, "Obstacles to Dislocation Motion," [Online]. Available: http://www.bss.phy.cam.ac.uk/~amd3/teaching/A_Donald/Crystalline_Solids_2.pdf. [Accessed 8 December 2013].

[16] D. C. Murray, *On Improving The Oxidation Resistance Of A Nickel-Based Superalloy Produced By Powder Metallurgy,* Master of Applied Science thesis, Department of Process Engineering and Applied Science, Dalhousie University, Halifax, 2012.

[17] J. Goldstein, D. E. Newbury, D. C. Joy, C. E. Lyman, P. Echlin, E. Lifshin, L. C. Sawyer and J. R. Michael, Scanning Electron Microscopy And X-Ray Microanalysis, 3rd ed., Plenum Press, 2003.

[18] D. Leadly, "SEM," 10 Dec 2010. [Online]. Available: http://www2.warwick.ac.uk/fac/sci/physics/current/postgraduate/regs/mpags/ex5/techniques/electronic/sem-copy/. [Accessed 7 September 2013].

[19] Australian Microscopy & Microanalysis Research Facility, "MyScope: Electron-matter interactions," 15 March 2013. [Online]. Available: http://www.ammrf.org.au/myscope/sem/background/concepts/interactions.php. [Accessed 20 8 2013].

[20] Muso, "File:EDX-scheme.svg," 12 8 2009. [Online]. Available: http://commons.wikimedia.org/wiki/File:EDX-scheme.svg. [Accessed 22 8 2013].

[21] D. B. Williams and C. B. Carter, Transmission Electron Microscopy: A Textbook for

Materials Science, Volume 3, New York: Springer Science+Business Media, LLC., 2009.

[22] "TEM Comparison," Nature, [Online]. Available: http://www.nature.com/nprot/journal/v7/n9/fig_tab/nprot.2012.096_T1.html.

[23] G. Haugstad, Atomic Force Microscopy: Understanding Basic Modes and Advanced Applications, Hoboken: John Wiley & Sons, Inc., 2012.

[24] OverlordQ, "Atomic force microscope block diagram," 6 October 2009. [Online]. Available: en.wikipedia.org/wiki/File:Atomic_force_microscope_block_diagram.svg. [Accessed 20 January 2013].

[25] D. Hurley, "Acoustics says "Nano, Nano" to Materials Characterization," 7 June 2006. [Online]. Available: http://www.acoustics.org/press/151st/Hurley.html. [Accessed 10 8 2013].

[26] "AFM Comparison," University of Guelph, [Online]. Available: http://www.chembio.uoguelph.ca/educmat/chm729/afm/compare.htm.

[27] I. Fuzman, E. Granda, R. Mendez, G. Lopez, J. Acevedo and D. Gonzalez, "Particle Size of Gamma Prime as a Result of Vacuum Heat Treatment of INCONEL 738 Super Alloy," *Journal of Materials Engineering and Performance,* vol. 22, no. 4, pp. 1143-1148, 2013.

[28] A. Baldan, "Review- Progress in Ostwald ripening theories and their applications to nickel-base superalloys; Part I: Ostwald ripening theories," *Journal of Materials Science,* no. 37,

pp. 2171-2202, 2002.

[29] D. A. Akinlade, W. F. Caley, N. L. Richards and M. C. Chaturvedi, "Development of a powder metallurgy (PM) nickel-base Superalloy," *Int. J. Powder Metall.,* no. 42, pp. 43-56, 2006.

[30] D. A. Akinlade, W. F. Caley, N. L. Richards and M. C. Chaturvedi, "Microstructural and Thermal Processing Effects on adding 1 and 3w/o Ti to a Powder Metallurgy Processed Quaternary Ni-Cr-Fe-Al Alloy," *Mat.Sci and Eng. A,* no. 528, pp. 996-1002, 2011.

[31] D. A. Akinlade, W. F. Caley, N. L. Richards and M. C. Chaturvedi, "Thermodynamic modelling of a 6w/o Al P/M processed Ni base superalloy," *WIT Trans. on Eng. Sciences,* vol. 57, pp. 85-94, 2007.

[32] D. A. Akinlade, W. F. Caley, N. L. Richards and M. C. Chaturvedi, "Microstructural Response of an Al-Modified Ni-Cr-Fe Ternary Alloy During Thermal Processing," *Mat.Sci and Eng. A,* no. 486, pp. 626-633, 2008.

[33] Advanced Surface Microscopy Inc., "Dimension 3100 AFM," [Online]. Available: http://www.asmicro.com/testweb/Equipment/Dimension-3100-AFM.htm. [Accessed 28 Febuary 2014].

[34] Element Collection, Inc, "Density for all the elements in the Periodic Table," [Online]. Available: http://www.periodictable.com/Properties/A/Density.al.html. [Accessed 28 January 2017].

Appendix A

Appendix A contains the raw data of hardness measurements for the statistical heat treatment (see Section 4.6), in the order performed.

Run #	**1**	**2**	**3**	**4**	**5**	**6**	**7**	**8**
Time (h)	12.5	12.5	12.5	5	20	12.5	12.5	17.8
Temp (°C)	900	900	900	900	900	1000	900	829.3
Hardness (HV)	374	328	330	316	350	349	315	312
	365	328	327	288	328	360	311	313
	333	314	302	308	325	368	348	315
	352	349	284	341	375	340	356	328
	400	344	335	316	319	391	348	275
	362	322	304	300	331	345	321	316
	347	335	304	354	364	367	341	316
	383	339	315	339	370	437	352	331
			334	327				

Run #	**9**	**10**	**11**	**12**	**13**	**14**	**15**	**16**
Time (h)	12.67	7.2	17.8	12.5	7.2	12.5	12.5	12.5
Temp (°C)	900	829.3	970.7	800	970.7	900	900	900
Hardness (HV)	324	305	322	349	347	333	330	300
	324	320	339	313	331	344	312	336
	394	324	378	335	334	336	331	298
	343	320	333	349	313	337	343	350
	393	307	375	327	334	353	312	321
	353	328	385	336	280	361	333	353
	327	316	373	316	316	355	358	311
	332	358	332	335	312	322	309	369

Appendix B

Appendix B contains the code used to obtain the hardness visualization in Figure 42.

```
%Data and error: X is time, Y is temperature, Z is hardness, uncert is
standard deviation

% Simplified Center Point Data
x= [5 20 12.5 17.8 7.2 17.8 12.5 7.2 12.5];
y= [900 900 1000 829 829 971 800 971 900];
z= [321 345 370 313 322 355 323 321 337];
uncert= [21.21 22.27 31.64 16.97 16.45 25.38 13.37 20.58 19.28];

%Creating the X and Y equally spaced vectors
xlin = linspace(min(x),max(x),16);
ylin = linspace(min(y),max(y),11);

%Creating the XY grid
[X,Y] = meshgrid(xlin, ylin);

%Creating the interpolated datapoints to stack on the [X,Y] grid using cubic
Z = griddata(x,y,z,X,Y,'cubic');

%Drawing the 3D mesh and plot with labels
mesh(X,Y,Z)
axis ([4 21 750 1050 300 400]); hold on
plot3(x,y,z,'.', 'MarkerSize',20)
view([-5, 45]);

%Create axis labels
xlabel('Time (h)','FontSize',20);
ylabel('Temperature (°C)','Rotation',-75,'LineWidth',3,'FontSize',20);
zlabel('Vickers Hardness','FontSize',20);

%putting the z-values above each data point
text(x+.2,y,(z+10),num2str(z(:)),'FontWeight', 'bold','FontSize',20)

%drawing error bars
for i=1:length(x)
    xV=[x(i); x(i)];
    yV=[y(i); y(i)];
    zMin= z(i)+uncert(i);
    zMax= z(i)-uncert(i);

    zV=[zMin, zMax];

    plot3(xV,yV,zV, '-k', 'LineWidth',2);
end
```

Appendix C

Appendix C contains the data and calculations used to obtain the % theoretical densities (see Section 4.8) used in Results Sections 5.4and 5.5.

Table 11: Theoretical alloy densities [34]

Element	ρ (g/cm^3)	Alloys & Composition	
		Ternary	TAS
Ni	8.908	79	73.865
Cr	7.14	12	11.22
Fe	7.874	9	8.415
Al	2.7		6
Si	2.33		0.5
Theoretical max ρ:		**8.60**	**8.22**

The theoretical maximum densities in Table 11 above are calculated using the "rule of mixtures" method.

Table 12: Green densities of elemental powder samples

Sample	400 uniaxial	500 uniaxial	400 cip
Temperature of Water (°C)	20.8	20.8	20.8
Density of Water (g/cm^3)	0.997983524	0.997983524	0.997983524
Mass in Air (g)	15.0435	15.1846	14.3995
Mass oiled (g)	15.1693	15.2562	14.4939
Mass in Water (g)	12.6967	12.8519	12.2834
Sample Density (g/cm^3)	6.07	6.30	6.50
%theoretical density	**73.9%**	**76.7%**	**79.1%**

Table 13: Green densities of masteralloy powder samples

Sample	500 uniaxial	400 cip
Temperature of Water (°C)	20.8	20.8
Density of Water (g/cm^3)	0.997983524	0.997984
Mass in Air (g)	15.0486	14.8843
Mass oiled (g)	15.184	14.9398
Mass in Water (g)	12.8392	12.5467
Sample Density (g/cm^3)	6.40	6.21
%theoretical density	**77.9%**	**75.5%**

Appendix D

Appendix D contains the summary of the raw data used for precipitate size and distribution analysis (Section 5.7).

Table 14: Summary of AFM Image Precipitate Data

Sample	Image Name	Particle Count	Image Area (nm^2)	Average Particle Diameter (nm)	γ' Volume Fraction
1	1A	205	240464	19.3	24.1
1	1B	171	300848	23.7	30.5
2	2A	133	237111	23.8	24.1
2	2B	121	257694	26.0	26.2
	3A				
3	3B	44	53931	19.8	17.7
3	3C	36	75748	25.9	26.3
3	3D	138	362059	28.9	36.0
3	3E	207	588922	30.1	26.6
3	3F	106	217727	25.6	22.1
4	4A	97	229724	27.5	23.3
4	4B	113	269355	27.5	27.5
5	5A	100	273432	29.5	27.7
6	6A	95	258480	29.4	25.8
6	6B	66	252491	34.9	25.2
6	6C	123	296102	27.7	29.4
6	6D	83	359953	37.2	36.0
6	6E	86	307132	33.7	30.6
6	6F	84	257463	31.2	25.7
AVERAGES		111. 6	268813	**27.9**	**26.9**